TDP-43 toxic gain of function links ALS, FTD and Alzheimer's Disease through splicing dysregulation

Welmoed van Zuiden[1,2*], Thea D Meimoun[1,2*], Chen Bar[1,2], Aviad Siany[1,2], Lihi Moshe[1,2], Nancy Yacovzada[1,2], Eviatar Weizman[3], Manuela Neumann[4,5], Aron S Buchman[6,7], Yanling Wang[6], David A Bennett[7], Jonathan D Glass[8], Adam N Trautwig[8], Nicholas T Seyfried[8], Johnathan Cooper-Knock[9], Eran Hornstein[1,2#]

[1]Department of Molecular Genetics, Weizmann Institute of Science, Rehovot, Israel

[2]Department of Molecular Neuroscience, Weizmann Institute of Science, Rehovot, Israel

[3]G-INCPM, Weizmann Institute of Science, Rehovot 7610001, Israel

[4]Department of Neuropathology, University of Tübingen, Tübingen, Germany

[5]Molecular Neuropathology of Neurodegenerative Diseases, German Center for Neurodegenerative Diseases, Tübingen, Germany

[6]Rush Alzheimer's Disease Center, Rush University Medical Center, Chicago, IL, USA

[7]Department of Neurological Sciences, Rush University Medical Center, Chicago, IL, USA

[8]Emory University School of Medicine, Atlanta, GA USA

[9]Sheffield Institute for Translational Neuroscience, University of Sheffield, Sheffield, S10 2HQ, UK

* These authors contributed equally

Corresponding Author: Eran.Hornstein@weizmann.ac.il

Abstract

Loss of nuclear TDP-43 splicing activity is a common feature across neurodegenerative diseases including amyotrophic lateral sclerosis (ALS) and frontotemporal lobar degeneration (FTLD), but its relevance to Alzheimer's disease (AD) remains unclear. Here, we show that TDP-43 pathology in AD is broadly associated with splicing abnormalities, including aberrant splicing of amyloid precursor protein (APP). TDP-43 drives the formation of elongated APP isoforms, disrupting alternative splicing across ALS, FTLD-TDP and AD, providing a compelling mechanism for a long-standing observation of APP isoform dysregulation. We further establish a mechanistic link between TDP-43, APP splicing, and Aβ pathology. Surprisingly, the disruption to alternative APP splicing is mediated by a toxic gain of cytoplasmic TDP-43 function, rather than loss of its nuclear role. Using proximity proteomics and base editing in human iPSC-derived neurons, we show that TDP-43 pathology causes cytoplasmic co-sequestration of splicing regulators SCAF11, SRSF5, and TIAL1. Knockdown of these regulators also results in APP mis-splicing and increased Aβ burden, without affecting other TDP-43 targets such as STMN2 or UNC13A. Together, our findings suggest that TDP-43-mediated splicing dysfunction upstream of APP contributes to the pathogenesis of seemingly disparate neurodegenerative diseases, uniting AD and ALS/FTLD-TDP through a shared molecular mechanism.

Introduction

Dysregulation of alternative splicing has been broadly implicated in the pathogenesis of several neurodegenerative disorders, including ALS, FTD and AD [1,2]. TDP-43, encoded by the TARDBP gene, is a ubiquitous DNA- and RNA-binding protein (RBP) that localizes to the nucleus, where it regulates RNA processing in multiple ways, including splicing [3,4]. In nearly all cases of amyotrophic lateral sclerosis (ALS) and up to 50% of frontotemporal lobar degeneration (FTLD) patients, TDP-43 forms insoluble cytoplasmic inclusions and is depleted from the nucleus [5–8], leading to widespread splicing disruption and the inclusion of cryptic exons in mRNAs such as cytoskeleton-related STMN2 and synaptic UNC13A [9–14]. Cryptic exon splicing of these targets is evident in several other neurodegenerative states including Alzheimer's Disease (AD) and Huntington's disease [9,10,13,15–18]. TDP-43 pathology is found in up to 57% of AD cases, where it correlates with disease severity [19,20] and is associated with increased Tau burden [21]. Critically, while alternative splicing is known to play a role in AD [22–28], the contribution of TDP-43 pathology to this remains largely unexplored.

The proteolytic processing of amyloid precursor protein (APP) into the neurotoxic Aβ peptide is thought to be a crucial step in the development of Alzheimer's disease (AD) [29,30]. Aβ aggregation is associated with elevated activity of APP-cleaving enzymes [31,32] or to certain genetic variants in APP [33–35]. Intriguingly, alternative splicing of exons 7 and 8 governs the production of three major APP isoforms: the neuron-enriched APP695 and two longer forms: APP751, and APP770. APP751 and APP770 contain the Kunitz protease inhibitor (KPI) domain while APP770 additionally includes the OX-2 domain [36,37]. Protein and mRNA levels of KPI(+)APP are elevated in AD and have been associated with increased Aβ production [38–42]. However, the mechanistic underpinning of alternative splicing of APP in AD is not well understood.

Here, we show that TDP-43 pathology is broadly associated with splicing abnormalities in AD including the regulation of APP alternative splicing. This finding extends across neurodegenerative diseases, suggesting a commonality for ALS/FTLD-TDP and AD. Moreover, this analysis reveals the mechanistic underpinning of APP isoform dysregulation that was originally reported several decades ago [38–42] that partially mediates Aβ pathology. Surprisingly, toxic gain of TDP-43 function, not loss of nuclear TDP-43 function, causes the shift in APP isoforms. We characterize the mechanism, which involves cytoplasmic co-sequestration of three other splicing regulators from the nucleus: SCAF11, SRSF5 and TIAL1. Taken together, TDP-43 pathology ties seemingly disparate neurodegenerative diseases together via splicing dysfunction.

Results

TDP-43 pathology is associated to splicing abnormalities in Alzheimer's Disease

To investigate whether TDP-43 pathology contributes to alternative splicing in AD, we analyzed RNA sequencing data of post-mortem dorsolateral prefrontal cortex (DLPFC) tissue samples from the Religious Orders Study and Rush Memory and Aging Project (ROSMAP [43], Synapse: syn4164376 [44]). We performed splicing analysis with MAJIQ [45], comparing patients clinically diagnosed with AD dementia (N = 253) to controls without cognitive impairment (N = 201), and comparing brain tissues with TDP-43 pathology (N = 150) to those without (N = 150) (demographics in **Table 4 (Methods)** and sample IDs in **Supplementary Table 1**). In total, aberrant splicing events were found in 2890 mRNAs in AD cases compared to controls, and in 1596 mRNAs in tissue samples with TDP-43 pathology compared to those without (|deltaPSI| > 0.02, signifying the change in percent spliced in (PSI) between conditions, and P-value < 0.05; **Supplementary Table 2**). A significant portion of the mRNAs alternatively spliced in AD was also alternatively spliced upon TDP-43 pathology (Fisher's exact P-value < 0.0001, **Figure 1A**). This includes the majority of mRNAs previously reported to be mis-spliced in AD by Raj et al. [22]. Moreover, the exact splice junctions alternatively used in AD significantly overlapped with those alternatively used upon TDP-43 pathology (Fisher's exact P-value < 0.0001, **Figure 1B**). Notably, the magnitude and direction of splicing changes at these overlapping junctions were remarkably concordant (Pearson r = 0.934, P < 0.0001, **Figure 1C**), strongly implicating TDP-43 pathology as a major driver of splicing dysregulation in AD.

Among the mRNAs mis-spliced in AD and upon TDP-43 pathology is PICALM, which is genetically associated to AD [46] and was previously reported to be mis-spliced in AD [22]. Usage of the splice junction between exons 12 and 14 was increased by 8% in AD (P-value < 0.001) and by 6% upon TDP-43 pathology (P-value < 0.01, **Figure 1D**). Accordingly, the splice junction between exons 13 and 14 was used 9% less in AD (P-value < 0.001) and 6% less upon TDP-43 pathology (P-value < 0.05, **Figure 1D**). Other highly mis-spliced targets include NCAM1 (**Supplementary Figure 1A**) and KIDINS220 (**Supplementary Figure 1B**), both of which have been implicated in AD [47–49].

We next asked whether TDP-43 pathology could contribute to aberrant splicing of the microtubule-associated protein Tau (MAPT) gene. More than 30 isoforms are predicted to arise as a result of alternative splicing of MAPT mRNA, but most variation comes from altered inclusion of exons 2, 3 and 10 [50]. Analysis of ROSMAP data revealed that the junction between exons 2 and 5 was used 5% more in AD (P-value <

126 0.05) and 5% more upon TDP-43 pathology (P-value < 0.05), while inclusion of exon 3 was decreased with
127 5% in both comparisons (P-value < 0.05, **Figure 1E**). Thus, TDP-43 pathology broadly affects splicing of key
128 effectors of AD.
129
130 **Amyloid precursor protein is aberrantly spliced upon TDP-43 pathology**
131 Alternative splicing of amyloid precursor protein (APP) has been recognized in AD for more than three
132 decades [38–41,51,52], however, its mechanistic underpinnings remain unknown. Our results demonstrate that
133 APP mRNA is significantly mis-spliced both in AD and when there is TDP-43 pathology (MAJIQ P-value <
134 0.0001, **Figure 1F, G**). The junction between exons 6 and 9, which produces isoform APP695 (**Figure 1F**),
135 was used 5% less in samples with TDP-43 pathology compared to those without (P-value < 0.01). This was
136 accompanied by a reciprocal 5% increase in splice events involving exon 7 or exons 7-and-8 inclusion,
137 leading to APP751 or APP770 formation, respectively (P-values < 0.01, **Figure 1F, G** and **Supplementary**
138 **Table 3**).
139
140 An orthogonal bioinformatic approach, with RNA-Seq by Expectation Maximization RSEM [53] (N=505)
141 revealed 20% reduced expression of APP695 (P-value < 0.001) and a higher APP751+APP770 expression
142 (P-value < 0.01) in samples with TDP-43 pathology, relative to those without (**Supplementary Figure 1C**).
143 In addition, abundance of two peptides mapping specifically to the longer APP isoforms (APP751 and
144 APP770) was increased in ROSMAP samples with TDP-43 pathology compared to those without (P-values
145 < 0.05, **Figure 1H**), confirming APP isoform dysregulation at the protein level.
146
147 To test whether the association of TDP-43 pathology to APP splicing is present in other neurodegenerative
148 conditions, we next analyzed RNA sequencing data from neuronal nuclei displaying TDP-43 pathology in
149 ALS/FTLD-TDP human brains [54] (**Figure 1I**). Splicing analysis comparing TDP-43-positive to TDP-43-
150 depleted nuclei revealed 8837 aberrant splicing events (|deltaPSI| > 0.1 and P-value < 0.1) in 2947 genes,
151 including UNC13A and STMN2 (**Supplementary Table 2**). Approximately one third of the mRNAs
152 alternatively spliced in AD associated to TDP-43 are also evident in ALS/FTLD-TDP (Fisher's exact P-value
153 < 0.0001, **Supplementary Figure 1D**), suggesting a broad overlap in TDP-43–dependent splicing defects
154 across both diseases. In TDP-43-depleted nuclei, usage of the splice junction between APP exons 6 and 9
155 decreased by 10% compared to control nuclei (P-value < 0.0001, **Figure 1J** and **Supplementary Table 3**).
156

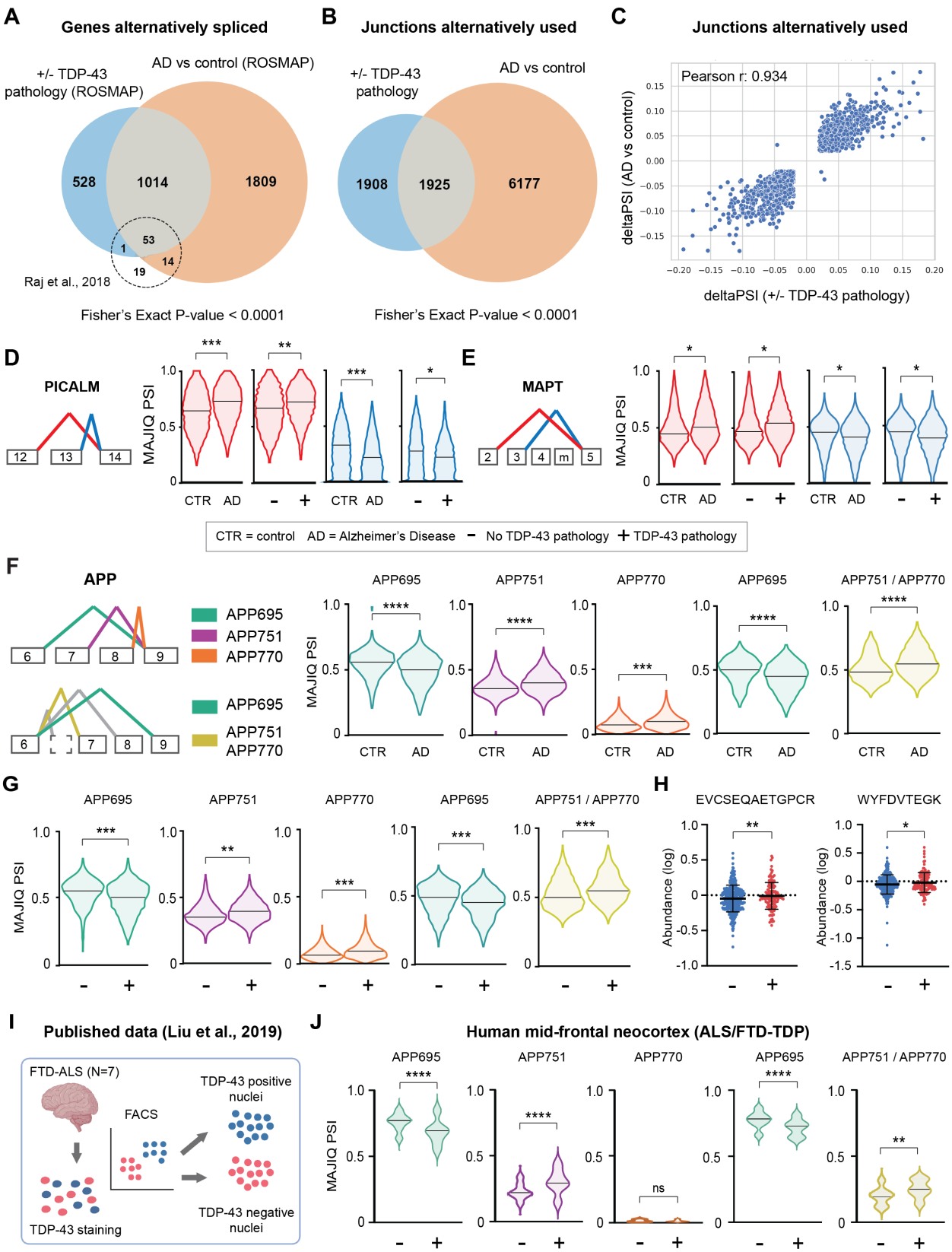
A
Genes alternatively spliced
+/- TDP-43 pathology (ROSMAP)
AD vs control (ROSMAP)
528
1014
1809
53
1
14
19
Raj et al., 2018
Fisher's Exact P-value < 0.0001
B
Junctions alternatively used
+/- TDP-43 pathology
AD vs control
1908
1925
6177
Fisher's Exact P-value < 0.0001
C
Junctions alternatively used
Pearson r: 0.934
deltaPSI (AD vs control)
deltaPSI (+/- TDP-43 pathology)
D
PICALM
12
13
14
MAJIQ PSI
CTR AD - + CTR AD - +
E
MAPT
2
3
4
m
5
CTR = control AD = Alzheimer's Disease - No TDP-43 pathology + TDP-43 pathology
F
APP
6
7
8
9
APP695
APP751
APP770
APP751 / APP770
G
H
EVCSEQAETGPCR
WYFDVTEGK
Abundance (log)
I
Published data (Liu et al., 2019)
FTD-ALS (N=7)
FACS
TDP-43 positive nuclei
TDP-43 negative nuclei
TDP-43 staining
J
Human mid-frontal neocortex (ALS/FTD-TDP)
ns

157

158 **Figure 1: TDP-43 pathology is associated with widespread mis-splicing in Alzheimer's Disease including in amyloid**
159 **precursor protein (APP).** MAJIQ [45] splicing analysis of bulk RNA-seq data from dorsolateral prefrontal cortex (DLPFC)
160 tissue from the ROSMAP study [44], comparing patients clinically diagnosed with AD (N = 253) to controls with no
161 cognitive impairment (N = 201), and comparing brain tissues with TDP-43 pathology (N = 150) to those without (N =
162 150) (+/- TDP-43 pathology). Venn diagrams display the overlap in **(A)** mRNAs mis-spliced in both analyses (Fisher's
163 exact P-value < 0.0001) or **(B)** exact MAJIQ splice junctions alternatively used in both comparisons (Fisher's exact P-
164 value < 0.0001). **(C)** A scatter plot of change in percent spliced in (deltaPSI) per specific splice junction in TDP-43
165 pathology, relative to TDP-43 negative AD brains (x-axis) vs AD pathology relative to controls without cognitive
166 impairment (y-axis). Pearson r = 0.934, P < 0.0001. Schematic of the splice junctions detected by MAJIQ in **(D)** PICALM
167 exons 12-14 or **(E)** MAPT exons 2-5, and corresponding percent spliced-in (PSI) values in ROSMAP AD (N = 253) versus
168 control (CTR) samples (N = 201) and samples with TDP-43 pathology (+, N = 150) versus those without (-, N = 150) [43].
169 Median PSIs per group are indicated. **(F)** Schematic of the splice junctions detected by MAJIQ in APP exons 6-9 and
170 the corresponding known isoforms, and corresponding PSI values in ROSMAP samples comparing AD versus control
171 samples or **(G)** tissue samples with TDP-43 pathology (+) versus those without (-). Median PSIs per group are
172 indicated. **(H)** Abundance of two peptides mapping specifically to longer APP isoforms APP751 and APP770
173 comparing ROSMAP samples with TDP-43 pathology (+) versus those without (-). Values are log-transformed. P-
174 values ** < 0.01, * < 0.05, one-way ANOVA. **(I)** Diagram of the experimental setup of the published study of Liu et
175 al. [54], in which neuronal nuclei were isolated from ALS/FTLD-TDP brains and sorted to separate between TDP-43-
176 positive nuclei without pathology and TDP-43-negative nuclei (with pathology). **(J)** MAJIQ percent spliced-in (PSI)
177 values of the APP exons 6-9 splice junctions in TDP-43-positive nuclei without pathology (-) vs TDP-43-negative nuclei
178 (with pathology, +). Data from 7 cases, 35,000 to 100,000 nuclei pre-sorting per case. MAJIQ P-values: ** < 0.01, ***
179 < 0.001, **** < 0.0001, Wilcoxon test.
180
181 Accordingly, the junction between exons 7 and 9 was used 10% more (P-value < 0.0001, **Figure 1J**). In
182 addition, the splice junction between exons 6 and 7 was used 7% more in TDP-43-depleted nuclei,
183 resulting in an increase in isoforms APP751 and APP770 compared to control (P-value < 0.01, **Figure 1J**).
184 These results, arising from direct comparison between pure TDP-43-positive and TDP-43-negative
185 populations, confirm APP mis-splicing downstream of TDP-43 pathology and extend the observations to
186 ALS/FTLD-TDP, suggesting a shared molecular mechanism across neurodegenerative diseases.
187
188 **TDP-43 pathology and consequent APP mis-splicing lead to increased amyloid-β pathology**
189 Previous reports suggest a correlation between elevated protein and mRNA levels of KPI(+)APP (APP751
190 and APP770) and increased amyloid-β (Aβ) production in AD [38–40]. Thus, we examined whether TDP-43
191 pathology could lead to increased Aβ through APP mis-splicing. First, we tested the correlation between

192 TDP-43 pathology, APP isoforms, and Aβ in human post-mortem brain tissue. ROSMAP DLPFC samples
193 that displayed TDP-43 pathology also showed ~1.4-fold increased Aβ pathology by immunohistochemistry
194 (P-value < 0.0001, **Figure 2A**) as well as mass spectrometry (P-value < 0.001**, Figure 2B**). In addition,
195 binning samples by their ratio of APP770+APP751 over APP695 mRNA levels (**Methods**) found a
196 correlation between higher (APP770+APP751)/APP695 ratio and elevated Aβ pathology (P-value < 0.05,
197 **Figure 2C, D**). Although this correlation exists regardless of TDP-43 pathology status, the increase in Aβ
198 pathology was significantly larger in the presence of TDP-43 pathology (P-value < 0.0001, **Figure 2E**).
199
200 Next, we conducted causal chain mediation analyses to quantify whether APP isoform levels explain part
201 of the relationship between TDP-43 pathology and Aβ pathology in DLPFC samples from the ROSMAP
202 study [43] (**Table 1**). The total effect of TDP-43 on Aβ (noted c) is the overall impact of TDP-43 on Aβ -
203 including both direct (noted c') and mediated effects (noted a and b) - where c=c'+ab. First, we modeled
204 the total effect of TDP-43 on Aβ using linear regression of Aβ over TDP-43 and found that TDP-43 is a
205 significant predictor and positively correlated, explaining 6.5% of the variance in Aβ (coefficient c = 0.4029,
206 P-value < 0.0001). Secondly, the relationship between TDP-43 pathology and different APP isoforms
207 (noted a) was tested: TDP-43 is positively correlated with APP770 levels (coefficient a = 1.874, P-value <
208 0.0001) and with APP751+APP770 (coefficient a = 0.0465, P-value = 0.003), and negatively correlated with
209 APP695 (coefficient a = -21.8, P-value = 0.005). A positive correlation is also found between TDP-43 and
210 APP7701+APP695 (coefficient a = 0.047, P-value < 0.0001) as well as APP751+APP7701+APP695
211 (coefficient a = 0.051, P-value = 0.001). Lastly, to estimate mediation effects for the different APP isoforms,
212 we quantified the effect of APP on Aβ pathology while controlling for TDP-43 (**Table 1**). If c' (direct effect
213 of TDP-43 on amyloid beta) is reduced or non-significant when APP is added, then APP mediates the effect.
214 APP770, APP7701+APP695 and APP751+APP7701+APP695 are all mediating the effect of TDP-43 on Aβ,
215 with APP7701+APP695 mediating the largest proportion (0.08, P-value < 0.0001, **Table 1** and **Figure 2F**).
216 No significant mediation effect was found for APP695. Altogether, these results demonstrate that TDP-43
217 pathology strongly influences Aβ pathology and that at least part of this effect is mediated through
218 increased levels of APP770 and APP751 relative to APP695.
219

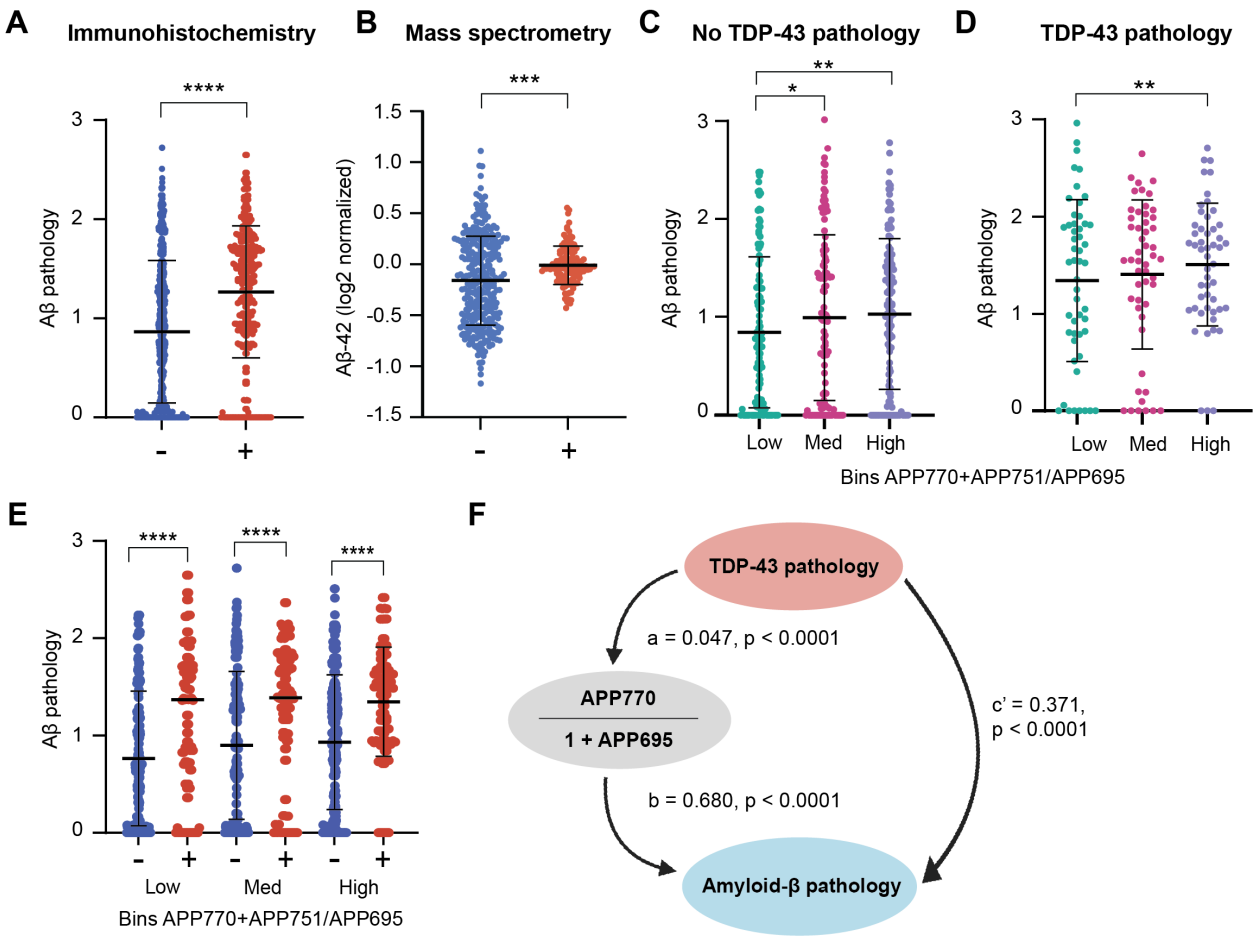

Figure 2: TDP-43 pathology and consequent APP mis-splicing lead to increased Aβ production. Aβ pathology in human DLPFC samples from the ROSMAP study [43] comparing samples with (+) or without (-) TDP-43 pathology as measured by **(A)** immunohistochemistry [55,56] (N=542) or **(B)** mass spectrometry [57] (N=410). Aβ pathology (immunohistochemistry) in human DLPFC samples from the ROSMAP study comparing samples with low, medium or high levels of APP751+APP770 relative to APP695 in **(C)** samples without TDP-43 pathology and **(D)** samples with TDP-pathology, and **(E)** samples with (+) or without (-) TDP-43 pathology binned by levels of APP751+APP770 relative to APP695. Lines and error bars represent mean and standard deviation. P-values ****< 0.0001, ***< 0.001, ** < 0.01, *< 0.05; unpaired two-sided t-test or one-way ANOVA with Dunnett's multiple comparisons test. **(F)** Diagram depicting the results of mediation analysis testing the effect of TDP-43 pathology on Aβ pathology mediated by APP770 levels relative to APP695 levels.

Table 1: Results of mediation analyses testing the effects of TDP-43 pathology and APP isoforms on Aβ pathology.

Hypothesized mediation pathway: TDP-43 → APP → Aβ		
Pathway	**Equation**	
TDP-43 → Aβ (without mediation)	$A\beta = \alpha_0 + c \cdot TDP43 + \varepsilon_0$	
TDP-43 → APP	$APP = \alpha_1 + a \cdot TDP43 + \varepsilon_1$	
$APP \rightarrow A\beta$ (when controlling for TDP-43)	$A\beta = \alpha_2 + c' \cdot TDP43 + b \cdot APP + \varepsilon_2$	
Total Effect (c) ≃ Direct effect (c') + Indirect effect ($a \cdot b$) 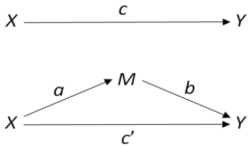		
$APP770$ as mediator		
Pathway	**Coefficient**	**P-value**
TDP-43 → Aβ (without mediation)	$c = 0.4029$	0.000
TDP-43 → $APP770$	$a = 1.874$	0.000
$APP770 \rightarrow A\beta$ (when controlling for TDP-43)	$b = 0.0152c'$ $= 0.3742$	0.000, 0.000
Significance of the indirect effect via bootstrapping: $a \cdot b = 0.028$, **95% CI** $[\mathbf{0.012}, \mathbf{0.047}]$		
Total Effect (c) = 0.429, **direct Effect (c')**= 0.374 $c' < c$ and $c' \neq 0 \Rightarrow APP770$ **is a partial mediator.** **Proportion Mediated** $\frac{(a \cdot b)}{c} = 0.071 = 7\%$.		
$\frac{APP770}{1+APP695}$ **as mediator**		

Pathway	Coefficient	P-value
TDP-43 → Aβ (without mediation)	$c = 0.4029$	0.000
TDP-43 → $\frac{APP770}{1+APP695}$	$a = 0.0471$	0.000
$\frac{APP770}{1+APP695} \rightarrow A\beta$ (when controlling for TDP-43)	$b = 0.6800$ $c' = 0.3705$	0.000 0.000
Significance of the indirect effect via bootstrapping: $a \cdot b = 0.032$, **95% CI** $[\mathbf{0.014}, \mathbf{0.052}]$		
Total Effect (c) = 0.403, **direct Effect (c')**= 0.371 $c' < c$ and $c' \neq 0 \Rightarrow \frac{APP770}{1+APP695}$ **is a partial mediator.** **Proportion Mediated** $\frac{(a \cdot b)}{c} = 0.080 = 8\%$		
$\frac{\boldsymbol{APP751+APP770}}{\boldsymbol{1+APP695}}$ **as mediator**		
Pathway	**Coefficient**	**P-value**
TDP-43 → Aβ (without mediation)	$c = 0.4029$	0.000
TDP-43 → $\frac{APP571+APP770}{1+APP695}$	$a = 0.0512$	0.001
$\frac{APP751+APP770}{1+APP695} \rightarrow A\beta$ (when controlling for TDP-43)	$b = 0.2390$ $c' = 0.3904$	0.020 0.000
Significance of the indirect effect via bootstrapping: $a \cdot b = 0.012$, **95% CI** $[\mathbf{0.001}, \mathbf{0.025}]$		
Total Effect (c) = 0.403, **direct Effect (c')**= 0.390 $c' < c$ and $c' \neq 0 \Rightarrow \frac{APP751+APP770}{1+APP695}$ **is a partial mediator.** **Proportion Mediated** $\frac{(a \cdot b)}{c} = 0.030 = 3\%$		

Cytoplasmic gain of toxic function, not loss of nuclear TDP-43 function, leads to APP mis-splicing

We next asked whether the loss of TDP-43 per se is associated with alternative splicing of APP. Analysis of RNA sequencing data of TDP-43 knockdown (KD) in iPSC-derived neurons [10] did not reveal aberrant APP splicing (deltaPSI < 0.01, P-values > 0.6), **Figure 3A** and **Supplementary Table 3**). Similarly, no APP mis-

243 splicing was observed upon complete knockout of TDP-43 in HeLa cells [58] (deltaPSI < 0.01, P-values > 0.55,
244 **Figure 3B** and **Supplementary Table 3**). Furthermore, only 16% of the mRNA species that displayed
245 aberrant splicing in TDP-43-negative ALS/FTLD-TDP brain nuclei were affected by TDP-43 KD (**Figure 3C**).
246 Therefore, a substantial portion of the splicing changes observed in post-mortem tissue cannot be
247 explained solely by the loss of TDP-43 function and likely involve additional molecular mechanisms.
248
249 We hypothesized that APP splicing is affected by TDP-43 mislocalization to the cytoplasm, which is a core
250 feature of disease pathology, but is not observed after TDP-43 KD. To test this, we overexpressed a TDP-
251 43 construct carrying a mutagenized nuclear localization signal (NLS) - rendering it cytoplasmic - in iPSC-
252 derived neurons (iNs), as described before [59]. As a cytoplasmic overexpression control, we induced
253 neurons that overexpress a nuclear export signal (NES, **Figure 3D**). Next-generation RNA sequencing and
254 splicing analysis (**Supplementary Table 2**) revealed a 32% decrease in the usage of the APP695-specific
255 splice junction in TDP-43^{deltaNLS} relative to NES (P-value < 0.0001, **Figure 3E** and **Supplementary Table 3**).
256 In contrast, the usage of the APP751-specific splice junction was increased by 24% (P-value < 0.0001,
257 **Figure 3E**). Similarly, the junction between exon 6 and 7 was used 32% more (P-value < 0.0001, **Figure 3E**).
258 Quantification of the three major isoforms by reverse transcription PCR (RT-PCR) (**Figure 3F**) verified a
259 significant 19% reduction in APP695 (P-value < 0.01, **Figure 3G**) and a concomitant 4-fold increase in
260 APP770 in TDP-43^{deltaNLS} (P-value < 0.00001, **Figure 3G**). These observations correlate with aberrant APP
261 splicing and TDP-43 pathology in human ALS/FTLD-TDP and AD brains. Finally, about 15% of the mRNAs
262 mis-spliced upon TDP-43 pathology in ALS/FTLD-TDP postmortem tissue [54] were also mis-spliced in TDP-
263 43^{deltaNLS} neurons (**Figure 3H**). This number is in the same ballpark of TDP-43 KD models, suggesting toxic
264 gain-of-function through mislocalization similarly contributes to splicing defects in ALS/FTLD-TDP.
265
266 **The mislocalization of splicing regulators upon cytoplasmic TDP-43**
267 Since many splicing abnormalities associated with ALS/FTLD-TDP could not be explained solely by the
268 nuclear loss of TDP-43, we hypothesized that additional splicing regulators are mislocalized with TDP-43
269 to the cytoplasm. To test this, we performed nucleo-cytoplasmic fractionation and mass spectrometry
270 using induced neurons expressing either TDP-43^{deltaNLS} or NES (**Figure 4A** and **Supplementary Table 4**). The
271 nuclear proteins Lamin-B1 and HDAC1 were highly enriched in the nuclear fraction of both TDP-43^{deltaNLS}
272 and the control NES cell lines (log2FC = 5.7 / 5.1, FDR = 0; **Supplementary Figure 2A**). In addition, analysis
273 of the top 200 most enriched or depleted proteins in the nucleus, using the gene ontology database [60,61]
274 confirmed proper separation of the nuclear and cytoplasmic fractions (**Supplementary Figure 2B, C**).

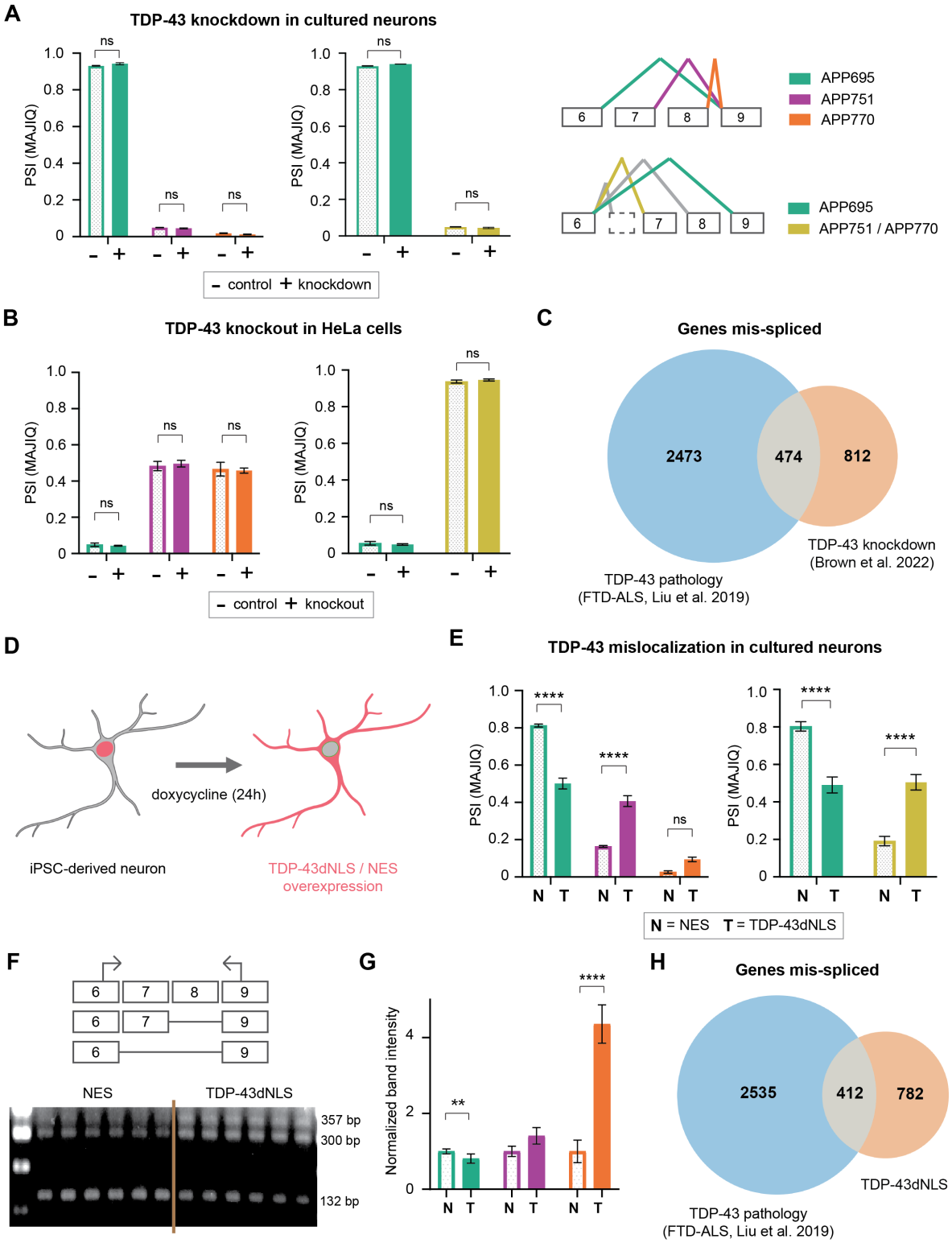
A
TDP-43 knockdown in cultured neurons
PSI (MAJIQ)
ns
- control + knockdown
APP695
APP751
APP770
APP695
APP751 / APP770
B
TDP-43 knockout in HeLa cells
- control + knockout
C
Genes mis-spliced
2473
474
812
TDP-43 knockdown
(Brown et al. 2022)
TDP-43 pathology
(FTD-ALS, Liu et al. 2019)
D
doxycycline (24h)
iPSC-derived neuron
TDP-43dNLS / NES
overexpression
E
TDP-43 mislocalization in cultured neurons
****
N = NES T = TDP-43dNLS
F
NES
TDP-43dNLS
357 bp
300 bp
132 bp
G
Normalized band intensity
**
****
H
Genes mis-spliced
2535
412
782
TDP-43dNLS
TDP-43 pathology
(FTD-ALS, Liu et al. 2019)

275

276

Figure 3: Gain of toxic function of cytoplasmic TDP-43 mislocalization causes APP mis-splicing. Percent spliced in (PSI) of splice junctions corresponding to the 3 main APP isoforms as determined by RNAseq and MAJIQ [45] in **(A)** TDP-43 knockdown (KD) in cultured neurons [10], or **(B)** knockout in HeLa cells [58]**. (C)** Venn diagram of alternatively spliced mRNAs in ALS/FTLD-TDP- post-mortem neuronal nuclei displaying TDP-43 pathology [54] and TDP-43 KD in cultured neurons [10]. **(D)** Diagram of experimental setup: iPSCs carrying transgenes were differentiated into day 8 cortical neurons [98], at which point NLS-mutated TDP-43 (TDP-43^{deltaNLS}) or nuclear export signal (NES) expression was induced with doxycycline. **(E)** MAJIQ PSI values of splice junctions corresponding to the 3 main APP isoforms in cultured neurons expressing NES or TDP-43^{deltaNLS}. P-values **** < 0.0001. **(F)** Gel electrophoresis of reverse transcription PCR products from APP mRNA isoforms in induced neurons that express either NES or TDP-43^{deltaNLS} and **(G)** corresponding quantification of PCR band intensities (arbitrary units). P-values ****< 0.0001, **< 0.01; unpaired two-sided t-test. **(H)** Venn diagram of alternatively spliced mRNAs in ALS/FTLD-TDP post-mortem neuronal nuclei displaying TDP-43 pathology [54] and in cultured neurons expressing TDP-43^{deltaNLS}.

Expression of TDP-43^{deltaNLS} was associated with the cytoplasmic enrichment of 173 proteins, relative to the cytoplasm of NES control neurons (FDR < 0.05, FC > 2; **Figure 4B**). TDP-43 itself was among the most enriched proteins with a 6.5-fold higher cytoplasmic expression in TDP-43^{deltaNLS} (FDR = 0.017, **Figure 4B**). Additionally, 20 of the mislocalized proteins are known to be involved in regulation of splicing: CELF1 [62–64], CPSF7 [65], CRIPT [66], DDX17 [67–69], DHX16 [70], ERH [71,72], FAM98B [73], HNRNPLL [74–77], LGALS3 [78,79], NONO [80,81], PSPC1 [81], PTBP2 [82], SNRPC [83,84], SRSF1 [85–88], SRSF2 [87–90], SRSF4 [87,88,91], SRSF5 [87,88,92,93], SRSF6 [87,88,92,94], SUPT6H [95] and U2SURP [96,97]. TDP-43^{deltaNLS} increased the cytoplasmic-to-nuclear ratio of these 20 splicing regulators relative to NES -expressing neurons (**Figure 4C**), suggesting that additional splicing regulators might be mislocalized to the cytoplasm, together with TDP-43, in human neurons.

Proximity labeling proteomics reveals additional cytoplasmic interactors of TDP-43

To elucidate the molecular mechanism related to aberrant splicing downstream of cytoplasmic TDP-43 localization, we characterized the proteins in the vicinity of the cytoplasmic TDP-43. To do this, we leveraged an existing proximity labeling proteomics dataset we recently obtained using TDP-43^{deltaNLS}-APEX neurons [59] (**Figure 4D**). APEX facilitates free radical formation upon exposure to hydrogen peroxide (H2O2), generating biotin-phenol (BP) radicals that attach to neighboring biomolecules. In this dataset, sodium arsenite stress was included as a treatment to model TDP-43 condensation. TDP-43 partially relocalized into biomolecular condensates and co-localized with stress granule marker G3BP1 in induced neurons that were treated with sodium arsenite (250 uM, 90 minutes), (**Supplementary Figure 3**), consistent with previous reports [99–106].

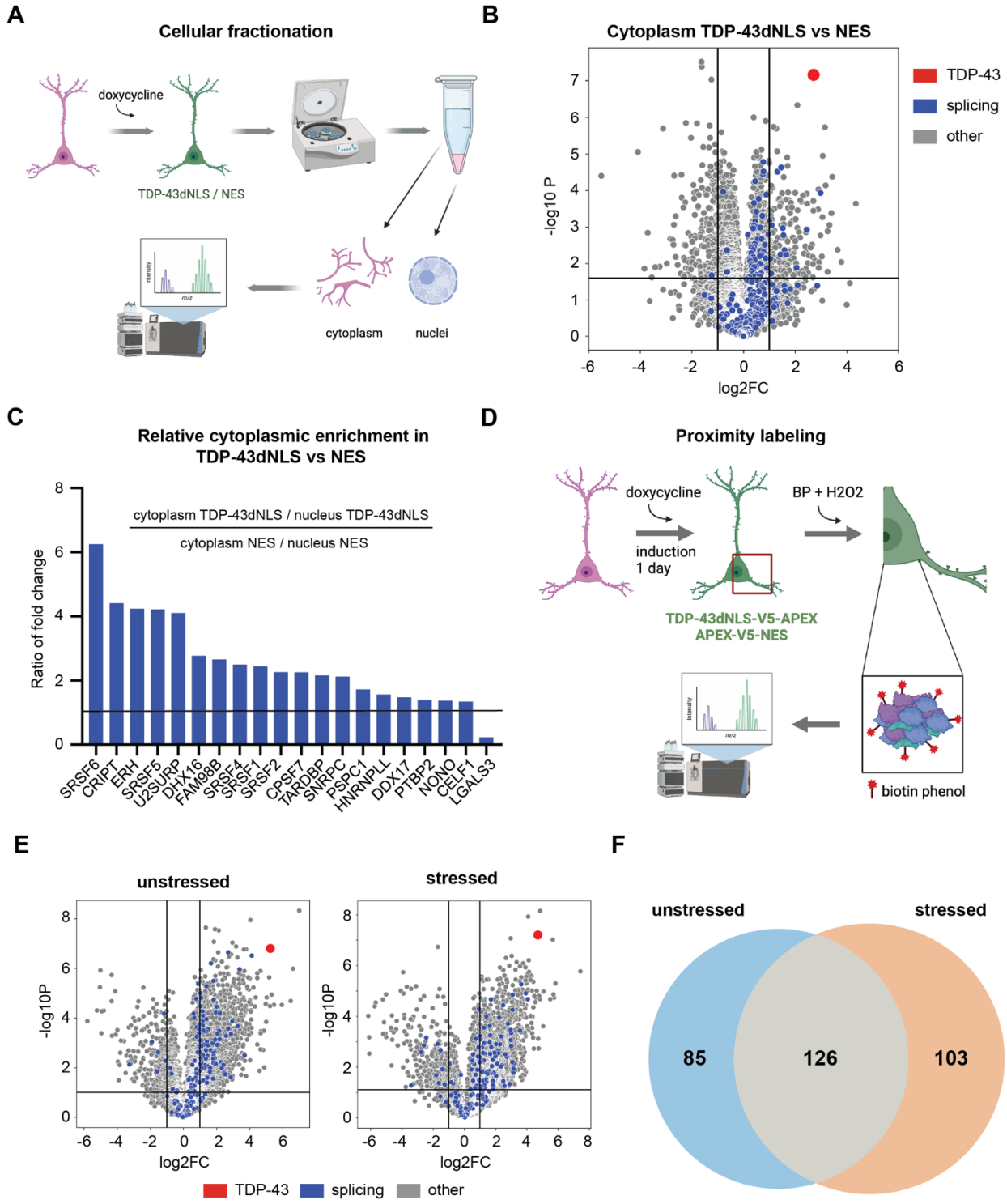
A
Cellular fractionation
doxycycline
TDP-43dNLS / NES
cytoplasm
nuclei
B
Cytoplasm TDP-43dNLS vs NES
TDP-43
splicing
other
-log10 P
log2FC
C
Relative cytoplasmic enrichment in TDP-43dNLS vs NES
cytoplasm TDP-43dNLS / nucleus TDP-43dNLS
cytoplasm NES / nucleus NES
Ratio of fold change
SRSF6
CRIPT
ERH
SRSF5
U2SURP
DHX16
FAM98B
SRSF4
SRSF1
SRSF2
CPSF7
TARDBP
SNRPC
PSPC1
HNRNPLL
DDX17
PTBP2
NONO
CELF1
LGALS3
D
Proximity labeling
doxycycline
induction
1 day
BP + H2O2
TDP-43dNLS-V5-APEX
APEX-V5-NES
biotin phenol
E
unstressed
stressed
-log10P
log2FC
TDP-43
splicing
other
F
unstressed
stressed
85
126
103

314 **Figure 4: Probing cytoplasmic co-sequestration of splicing regulators by TDP-43. (A)** Schematic of the subcellular
315 fractionation method to measure protein content of cytoplasmic and nuclear fractions of TDP-43^{deltaNLS}- and NES-
316 expressing neurons. **(B)** Volcano plot depicting protein abundance in the cytoplasm of neurons expressing TDP-
317 43^{deltaNLS} compared to a cytoplasmic control construct (NES). Factors associated with the Gene Ontology term
318 'splicing' are shown in blue; TDP-43 itself is depicted in red. **(C)** Relative cytoplasmic enrichment of the 14 splicing
319 regulators in TDP-43^{deltaNLS} compared to control NES in human neurons. For each protein, the ratio of cytoplasmic to
320 nuclear expression in TDP-43^{deltaNLS} was divided to the ratio in NES. **(D)** Schematic of APEX proximity labeling in TDP-
321 43^{deltaNLS}- and NES-expressing neurons as reported in [59]. **(E)** Volcano plots of differential protein enrichment in TDP-
322 43^{deltaNLS} samples (right) versus NES samples (left), with TDP-43 shown in red and factors associated with the Gene
323 Ontology term 'splicing' in blue. **(F)** The potential TDP-43 interactors were consistently found in two different
324 experiments in both unstressed and/or stressed conditions.
325
326 Reassuringly, TDP-43 itself was among the most enriched proteins (FDR = 0, log2FC = 5.24; red dots in
327 **Figure 4E** and **Supplementary Figure 4A**). While the overall number of proteins identified in each
328 experiment was different, 211 proteins were detected in both experiments under basal growth conditions
329 (unstressed) and 229 proteins under stress (FDR, < 0.01, log2FC > 2, **Supplementary Table 5**). 126 proteins
330 were consistently associated with cytoplasmic TDP-43 regardless of stress state (**Figure 4F)**. Gene
331 Ontology (GO) pathway molecular function analysis revealed substantial enrichment of DNA- and RNA-
332 binding proteins (**Supplementary Figure 4B**), which aligns with known TDP-43 functions [3,4,107]. Among the
333 proteins associated with TDP-43 were 11 splicing regulators, including CELF2 [108], TIA1 and TIAL1
334 [109,110] (**Table 2**).
335
336 **Table 2: Splice regulators associated with TDP-43^{deltaNLS}.**

basal interactors only	interactors under stress only	interactors under basal and stress conditions
CELF2	CASC3	SCAF11
METTL3	ECD	TARDBP
TIAL1	IVNS1ABP	TIA1
	TTF2	
	ZCCHC8	

337
338
339

340 **Knockdown of splicing regulators associated with TDP-43 partially recapitulates TDP-associated**
341 **changes**
342 We next investigated whether the newly identified TDP-43 interactors play a role in splicing by generating
343 loss-of-function alleles (knockdown, KD), using a cytidine base editor [111] in human iPSCs that were
344 differentiated to cortical neurons. In total, we identified 31 splicing regulators in the fractionation and
345 proximity labeling experiments described above. Out of these, we shortlisted 8 proteins that are localized
346 mostly to the nucleus under basal conditions: CELF2 [112–116], CPSF7 [65], HNRNPLL [74–77], SCAF11 [117], SRSF5
347 [87,88,92,93], SUPT6H [95], TIA1 [109,110,118] and TIAL1 [118–120] (**Figure 5A**). TIA1 was included because of its genetic
348 association with ALS [121,122], and TIAL1 is its paralog and acts in close coordination [118,120,123,124]. The
349 introduction of premature stop codons led to downregulation of mRNA levels and plausibly prevented
350 the formation of full-length protein products (**Supplementary Figure 5**). Full RNA sequencing followed by
351 splicing analysis revealed differential usage (|deltaPSI| > 0.1, P-value < 0.1) of hundreds of splice junctions
352 upon KD of the eight splicing regulators (**Table 3** and **Supplementary Table 2**). TIA1 displayed the mildest
353 phenotype, although this is likely due to the fact that we could only generate a heterozygous KD
354 (generation of a homozygote was unsuccessful; **Table 3**).
355
356 **Table 3: Number of splice junctions with significantly different usage between conditions (|deltaPSI| >**
357 **0.1, P-value < 0.1).**

KD condition	Number of junctions that were included more / less upon KD
SRSF5 (homozygous)	2656 /2708
CPSF7 (homozygous)	1666 /1574
SUPT6H (homozygous)	1533 /1559
TIAL1 (homozygous)	1108 /1120
CELF2 (homozygous)	950 /943
HNRNPLL (homozygous)	903 /923
SCAF11 (homozygous)	870 /934
TIA1 (heterozygous)	691 /645

358
359 We next compared changes in splicing at previously reported TDP-43–dependent junctions, using data
360 from the literature [10,43,54,58,125,126], RNA-seq of neuronal cultures knocked down for eight splicing regulators
361 (**Table 3**), and control-induced neurons. Aberrant cryptic exon splicing was detected in STMN2 and
362 UNC13A upon TDP-43 KD and upon TDP-43 pathology in both ALS/FTLD-TDP and AD tissues (**Figure 5B**),

363 consistent with previous reports [9,10,13,15]. Interestingly, UNC13A was misspliced upon SRSF5 and SUPT6H
364 KD (**Figure 5B**), but the mis-splicing occurred at a different splice junction than what has been previously
365 reported in the literature [9,10]. In SRSF5 KD neurons, two events were significantly altered in UNC13A: one
366 mapping to canonical exon 7 and an unannotated exon identified by MAJIQ (hg38; chr19:17665549-
367 17665977, |deltaPSI| = 17%, P-value < 0.05), and another involving exon 37 and canonical exon 39 (hg38;
368 chr19:17623118-17623263, |deltaPSI| = 20%, P-value < 0.05) (**Supplementary Figure 6A**). The same mis-
369 splicing in exon 7 and an annotated exon occurred upon SUPT6H KD (|deltaPSI| = 18%, P-value < 0.05,
370 **Supplementary Figure 6B**). Each of these events was relatively rare, with only a few dozen reads mapping
371 to each junction. Reported mis-splicing events in MYO18A [125] and ANXA11 [126] were found upon KD of
372 several TDP-43-associated splicing regulators (**Figure 5B**). In the case of ANXA11 and APP, mis-splicing was
373 seen in post-mortem tissues and upon KD of splicing regulators, but not upon TDP-43 KD. This suggests
374 the nuclear loss of regulators, rather than the loss of TDP-43 itself, is causing aberrant splicing in these
375 mRNAs.
376
377 More broadly, when comparing significantly mis-spliced mRNAs(|deltaPSI| > 0.1, P-value < 0.1 in at least
378 one junction) across all conditions, KD of each of the 8 splicing regulators was associated to hundred and
379 sometimes hundreds of splicing events that arise with TDP-43 pathology [54] (Fisher's exact P-values <
380 0.0001, **Figure 5C**). A substantial fraction of the splicing events that are associated with TDP-43 pathology
381 in post-mortem tissue [54] are also observed as a consequence of the loss of specific splicing regulators.[54]
382 For example, 20% of the mRNAs that were mis-spliced in ALS/FTLD-TDP CNSare also alternatively spliced
383 upon SRSF5 KD (585 out of 2947 mRNAs, Fisher's exact P-value < 0.0001, **Figure 5C**). These results suggest
384 that mislocalization of TDP-43 to the cytoplasm leads to splicing defects not only because of the loss of
385 TDP-43 function from the nucleus, but at least in part because of the sequestration of other splicing
386 regulators from the nucleus.
387
388 **Knockdown of TDP-43-associated splicing regulators leads to APP mis-splicing and Aβ generation**
389 We next examined whether the loss of TDP-43-associated splicing regulators could cause the APP mis-
390 splicing observed upon cytoplasmic TDP-43 mislocalization (**Figure 3E**). Knockdown of TIAL1, SCAF11, and
391 SRSF5 led to an increase in the usage of the junction between APP exons 7 and 8 (P-values < 0.0001, **Figure**
392 **5D**, left and **Supplementary Table 3**), similar to what was observed in ALS/FTLD-TDP brains (**Figure 1G, I**).
393 In addition, the junction between exons 7 and 9 was used more upon TIAL1 KD (P-value < 0.05, **Figure 5D**,
394 right and **Supplementary Table 3**). This was verified with RT-PCR (P-values < 0.05, **Figure 5E**). These results

395 suggest that co-sequestration of splicing regulators from the nucleus along with TDP-43, impairs the
396 balance between APP isoforms towards APP751 and APP770.
397
398 Finally, to test how these changes ultimately affect Aβ, we stained cultured neurons for Aβ (**Figure 5F**).
399 We observed increased cytoplasmic Aβ intensity in TIAL1 and SCAF11 KD neurons compared to control (P-
400 values < 0.001 and < 0.0001, respectively, **Figure 5G**), but not in SRSF5 KD neuronal cultures. Furthermore,
401 the number of Aβ-positive puncta was increased in all three KD lines (P-values < 0.05, **Figure 5H**).
402 Altogether, these results suggest that dysregulation of splicing regulators, in addition to TDP-43 itself, may
403 contribute to the pathophysiology of neurodegenerative disorders.
404

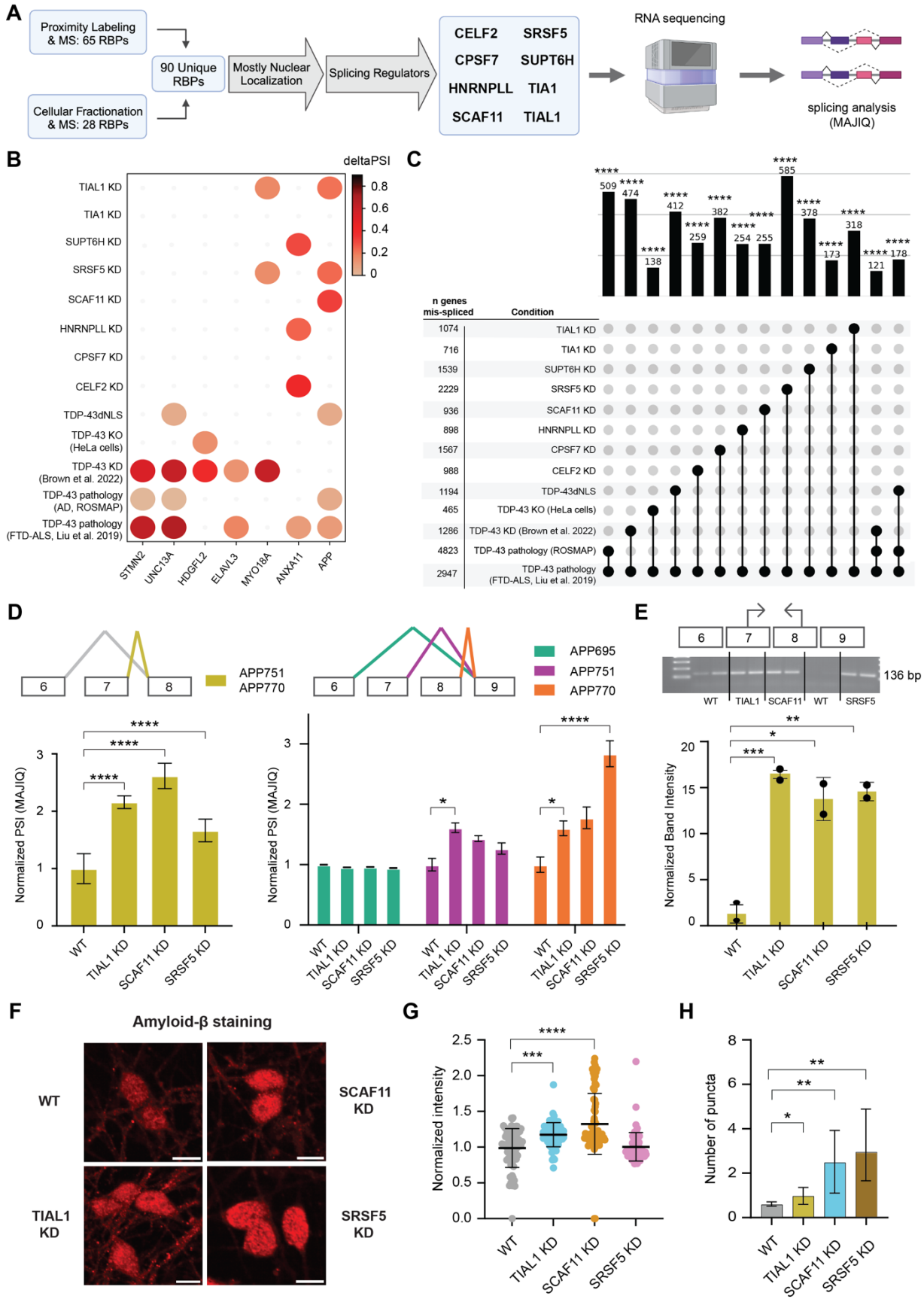
A
Proximity Labeling & MS: 65 RBPs
Cellular Fractionation & MS: 28 RBPs
90 Unique RBPs
Mostly Nuclear Localization
Splicing Regulators
CELF2 SRSF5
CPSF7 SUPT6H
HNRNPLL TIA1
SCAF11 TIAL1
RNA sequencing
splicing analysis (MAJIQ)
B
deltaPSI
TIAL1 KD
TIA1 KD
SUPT6H KD
SRSF5 KD
SCAF11 KD
HNRNPLL KD
CPSF7 KD
CELF2 KD
TDP-43dNLS
TDP-43 KO (HeLa cells)
TDP-43 KD (Brown et al. 2022)
TDP-43 pathology (AD, ROSMAP)
TDP-43 pathology (FTD-ALS, Liu et al. 2019)
STMN2
UNC13A
HDGFL2
ELAVL3
MYO18A
ANXA11
APP
C
n genes mis-spliced
Condition
D
APP751
APP770
APP695
Normalized PSI (MAJIQ)
WT
TIAL1 KD
SCAF11 KD
SRSF5 KD
E
136 bp
Normalized Band Intensity
F
Amyloid-β staining
WT
SCAF11 KD
TIAL1 KD
SRSF5 KD
G
Normalized intensity
H
Number of puncta

Figure 5: Knockdown of TDP-43-associated splicing regulators partially recapitulates ALS/FTLD-TDP-associated changes. (A) Schematic overview of the steps prioritizing 8 splicing regulators for KD in iPSCs. **(B)** Change in percent spliced in (deltaPSI) per splice junction as determined by MAJIQ in KD neurons compared to control. Junctions shown are those previously identified and characterized in the literature [125,126]. Significant events in UNC13A, STMN2, APP are annotated, specifically in AD and ALS patients with TDP pathology [10,43,54,125]. **(C)** Upsetplot comparison of shared splicing changes across conditions. Numbers on the left indicate the total number of mRNAs alternatively spliced, and numbers on the top indicate the number of mis-spliced mRNAs shared between datasets. P-values **** < 0.0001, Fisher's exact test comparing the significantly mis-spliced mRNAsin each dataset with those in TDP-43 pathology [54]. In the comparisons of three groups, a hypergeometric test was applied. **(D)** Alternative splicing of exons 6-9 of the APP mRNA as determined by MAJIQ in different KD neurons compared to control. Plots display percent spliced in (PSI) values normalized to control per junction. P-values * < 0.1, **** < 0.001. **(E)** Gel of reverse transcription PCR products from APP mRNA isoforms in induced neurons and corresponding quantification of PCR band intensities (arbitrary units). **(F)** Representative images of Aβ immunofluorescent staining in iPSC-derived neurons KD for TIAL1, SCAF11 or SRSF5. Corresponding quantification of **(G)** mean cytoplasmic intensity, normalized to WT, and **(H)** number of puncta normalized by cell number. Data from 3 repeats, 25 images per repeat are plotted; each point represents the average per **(G)** image or **(H)** well. P-values * < 0.05, ** < 0.01, *** < 0.001, **** < 0.0001.

Discussion

Our study establishes a new and unexpected connection across different neurodegenerative disorders. We show that TDP-43 pathology is broadly associated with splicing alterations in AD, including in the amyloid precursor protein (APP) gene. Both in AD and ALS/FTLD-TDP, TDP-43 pathology shifts the isoform balance towards APP751 and APP770. We show that this splicing alteration correlates with increased amyloid-β (Aβ) pathology, providing molecular evidence linking TDP-43 pathology to APP dysregulation and amyloid pathology. Functional validation using iPSC-derived neurons confirmed that cytoplasmic TDP-43 sequestration, rather than nuclear depletion, drives APP mis-splicing, suggesting an orthogonal but compatible mechanism to previously reported [9,10,13,17] loss of nuclear TDP-43 function. Finally, we report several RNA-binding proteins (RBPs) that are regulators of splicing and are co-sequestered with TDP-43. The splicing regulators potentially contribute to the dysregulation of splicing.

While TDP-43 proteinopathy was first linked with ALS and FTD [5], the presence of TDP-43 pathology in up to 57% of AD cases [20,127] and dysregulated TDP-43 in Huntington's disease (HD) [16] underscores its role in neurodegeneration. Abnormal levels or subcellular distribution of TDP-43 contributes to neuronal loss [100,128,129], and in AD, TDP-43 pathology correlates with worsened cognitive decline [130] and severity of pathology [131]. Thus, TDP-43 dysfunction might be a common key contributor to neurodegenerative diseases.

Splicing dysregulation is emerging as an important causal mechanism of neurodegeneration in diverse diseases. Splicing defects in AD have been documented previously [22–28] and offer a mechanistic explanation for genetic variants in novel and known AD genes, including APP [22]. However, the upstream causes remained unclear. Our data suggest that TDP-43 pathology is a significant driver of splicing abnormalities in AD, explaining a third of the total splicing changes in the AD brain. This goes far beyond any mechanism previously reported for the regulation of splicing in AD.

Accordingly, APP alternative splicing has been recognized for decades [36,37], but the underlying mechanism remained unclear. Our study provides a molecular handle on the regulation of APP splicing downstream of dysregulated TDP-43 in both ALS/FTLD-TDP- and AD.

Through mediation analysis, we show that TDP-43 pathology is associated with increased Aβ production, both directly and indirectly via shifting APP isoform towards APP751/770. This is consistent with previous

471 results from an AD mouse model, where injection of TDP-43 into the hippocampus increased amyloid
472 plaques and impaired spatial memory [132], and data from a small human cohort in which KPI(+)APP
473 correlated with neuritic plaque density [42]. In addition, previous *in vitro* results showed increased Aβ
474 production upon transfection with the longer APP isoforms compared to APP695 [133]. Together, our
475 discovery offers a molecular explanation for increased amyloid burden in TDP-43-positive AD cases [134,135].
476 Given that TDP-43 pathology is found in a significant subset of AD patients, this mechanism could have
477 broad implications for understanding and treating AD.
478
479 TDP-43-associated splicing pathology has been recently suggested to involve a loss-of-function
480 mechanism due to nuclear depletion [9,10,13,17]. Our data suggests a non-mutually exclusive role for toxic
481 cytoplasmic gain-of-function. We demonstrate that TDP-43 mislocalization does not necessarily disrupt
482 APP splicing directly, but rather due to sequestration of other splicing regulators, such as
483 SRSF5/TIAL1/SCAF11. This contrasts with STMN2 and UNC13A mis-splicing, which results directly from
484 nuclear TDP-43 depletion. The interplay between these two mechanisms highlights the complexity of TDP-
485 43 pathology. Future therapeutic strategies should consider targeting both nuclear restoration and
486 cytoplasmic toxicity to mitigate TDP-43-driven neurodegeneration.
487
488 Dysregulation of splicing regulators due to TDP-43 pathology provides a mechanistic explanation for
489 widespread splicing defects in neurodegenerative diseases. Loss of TDP-43 function through knockdown
490 or gain-of-function through mislocalization in culture, each explain about 15% of the mis-splicing
491 associated to TDP-43 pathology in ALS/FTLD-TDP postmortem tissue [54], suggesting that both mechanisms
492 can comparably contribute to splicing dysregulation downstream of TDP-43.
493
494 Furthermore, correction of splicing has been utilized as a therapeutic approach for spinal muscular
495 atrophy [136–138], and correction of STMN2 and UNC13A splicing is being developed as a potential
496 intervention strategy [139,140]. Therefore, redirecting APP splicing towards APP695 at the expense of
497 APP751/770 might be a justified therapeutic strategy as well.
498
499 Limitations: While our study provides strong evidence for TDP-43's role in APP splicing, several limitations
500 should be noted. Although we identify cytoplasmic splicing regulators co-sequestered with TDP-43, their
501 direct contributions to APP mis-splicing require further exploration. TIAL1 was shown to bind to APP
502 mRNA [141], which supports a function in APP splicing, but this was not demonstrated for SCAF11 and SRSF5

503 yet. Moreover, additional splice regulators not identified in this study may contribute to APP splicing
504 regulation. Furthermore, our proteomic analyses identified peptides specific to the longer APP isoforms,
505 but not to the APP695-specific peptide, which would enable a more complete protein-level analysis of
506 APP isoform ratios. The mechanism through which longer APP isoforms increase Aβ pathology also
507 remains to be investigated. Lastly, the TDP-43 pathology burden in the DLPFC in AD is typically lower
508 compared to other regions such as the amygdala and hippocampus [131,142,143]; thus, future studies might
509 benefit from including more TDP-43-enriched brain regions.
510
511 Our study identifies a novel mechanism linking TDP-43 pathology to APP alternative splicing and amyloid
512 pathology in AD and suggests that TDP-43 pathology is a unifying molecular feature linking seemingly
513 disparate neurodegenerative disorders. We provide evidence that TDP-43 mislocalization leads to
514 cytoplasmic sequestration of splicing regulators, driving an increase in APP751 and APP770 isoforms. This
515 mechanism underlying TDP-43 dysfunction suggests that ALS and FTD and amyloid-driven pathology in AD
516 may share common underlying molecular mechanisms. By establishing TDP-43 as an upstream regulator
517 of APP splicing, our findings offer new insights into the molecular convergence of neurodegenerative
518 diseases. Further work will be needed to determine whether these convergences occur early in the
519 evolution of these diseases or are a late common consequence of diverse causes of chronic CNS
520 neurodegeneration. Targeting this pathway may present novel therapeutic opportunities for both
521 ALS/FTLD-TDP and AD, highlighting the broader impact of splicing dysregulation in neurodegeneration.
522
523
524
525
526
527
528
529
530
531
532
533
534

535 **Supplementary Figures**

536

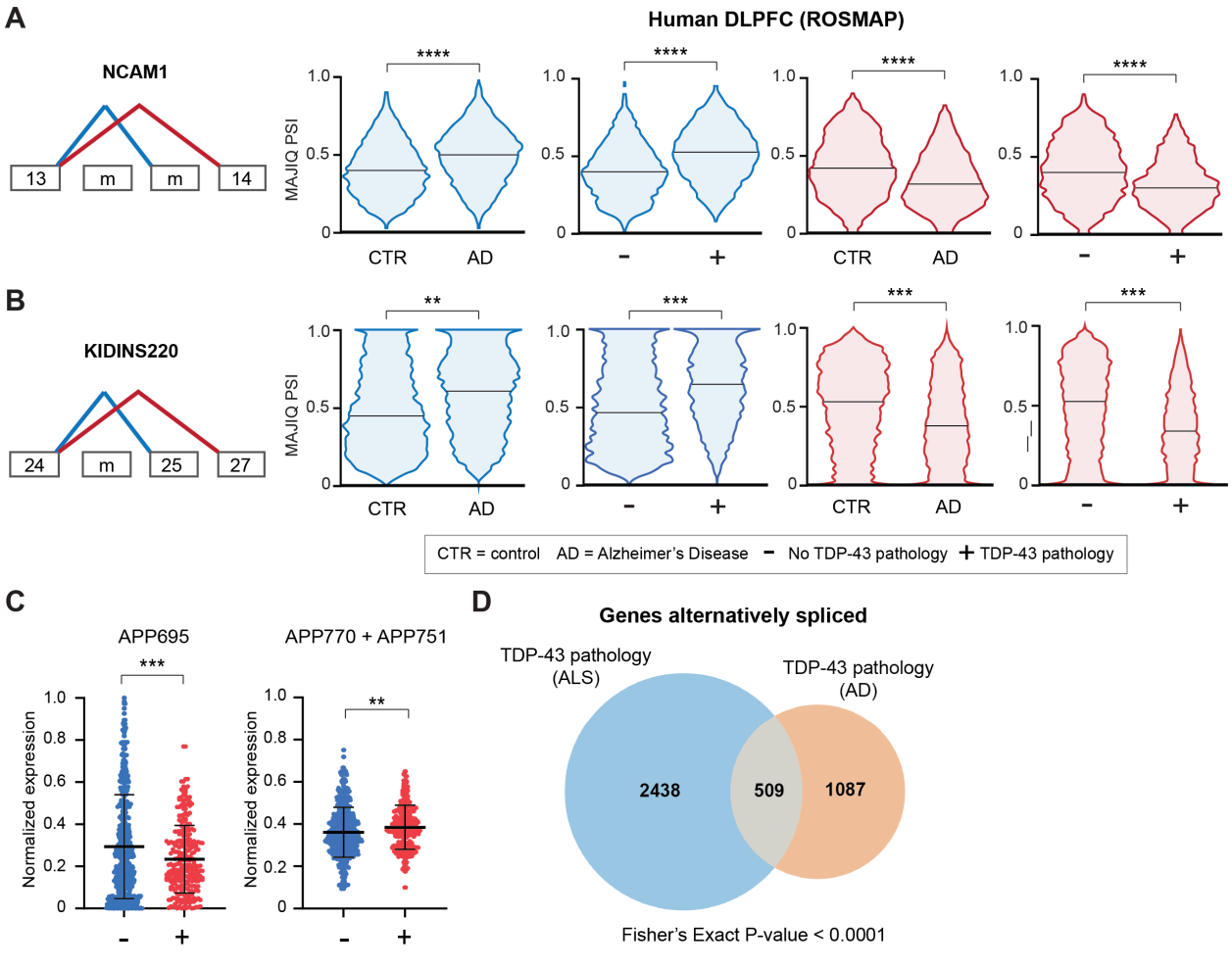

537

538

539 **Supplementary figure 1: Splicing aberrations downstream of TDP-43 pathology in human post-mortem tissue.**
540 Schematic of the splice junctions detected by MAJIQ in **(A)** NCAM1 exons 13-14 and **(B)** KIDINS220 exons 24-27, and
541 corresponding percent spliced-in (PSI) values in ROSMAP AD versus control samples and samples with TDP-43
542 pathology (+TDP-43) versus those without (-TDP-43) [43]. Numbers in the schematic indicate canonically annotated
543 exons, and 'm' represents novel exons identified by MAJIQ. Median PSIs per group are indicated. P-values **** <
544 0.0001, *** < 0.001, ** < 0.01; Wilcoxon test. **(C)** Normalized APP isoforms expression levels, estimated with RSEM
545 [53,144], of APP695 (without exons 7 and 8) and APP770 (containing exons 7 and 8) in human post-mortem dorsolateral
546 prefrontal cortex (DLPFC), comparing samples without TDP-43 pathology to those with TDP-43 pathology. Lines
547 represent the mean with SD. P-values ****< 0.0001, ***< 0.001, *< 0.05; unpaired two-sided t-test. **(D)** Overlap in
548 mRNAs mis-spliced in TDP-43 depleted nuclei vs TDP-43-positive nuclei from post-mortem cortical tissue [54] and
549 mRNAs mis-spliced upon TDP-43 pathology in ROSMAP DLPFC samples.

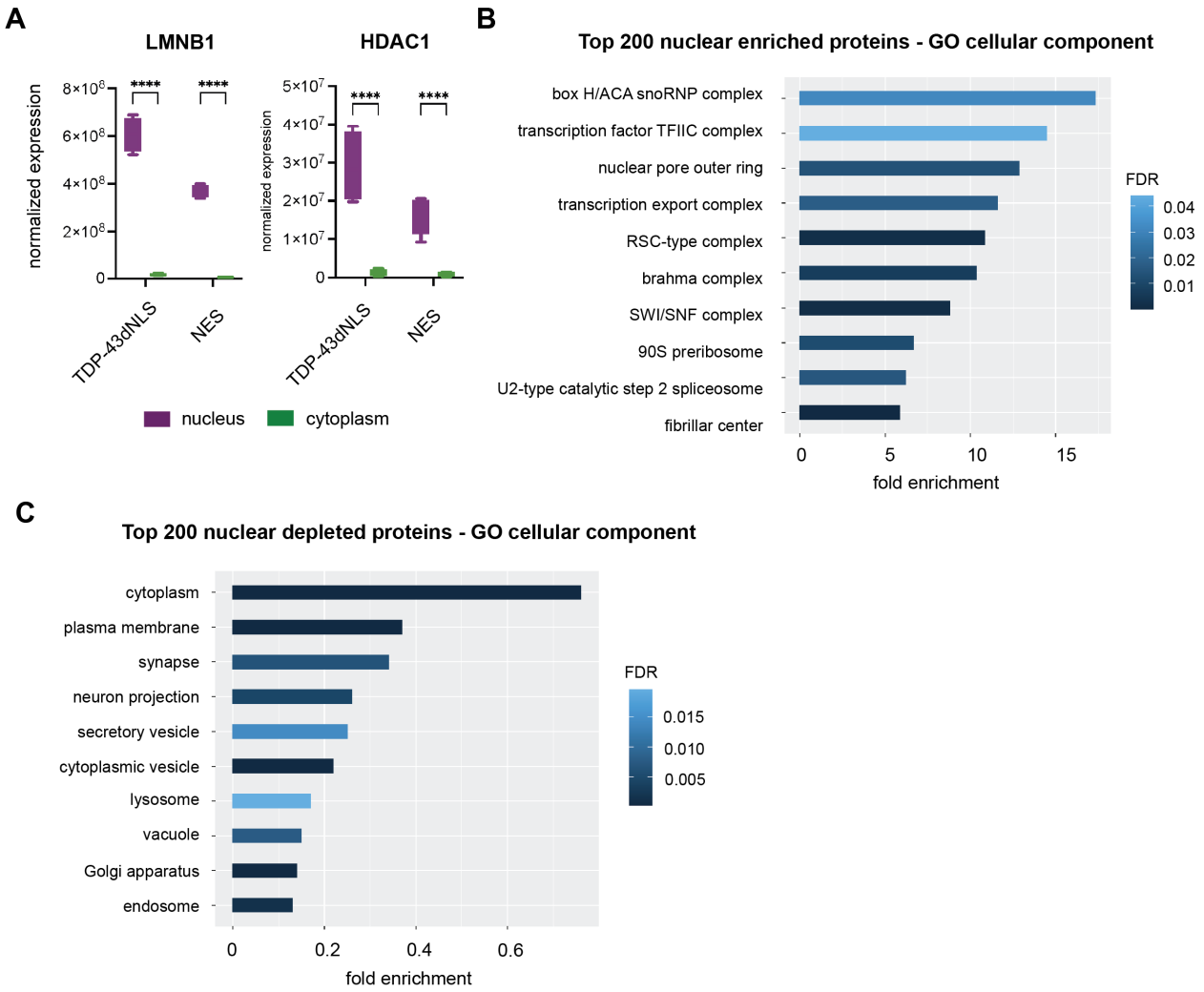

Supplementary Figure 2: Validation of separation between nuclear and cytoplasmic fractions. (A) Relative LMNB1 and HDAC1 intensity in each of the fractions in either NES- or TDP-43^{deltaNLS}-expressing neurons. Gene ontology [60,61] cellular component analysis of the top 200 most nuclear **(B)** enriched or **(C)** depleted proteins.

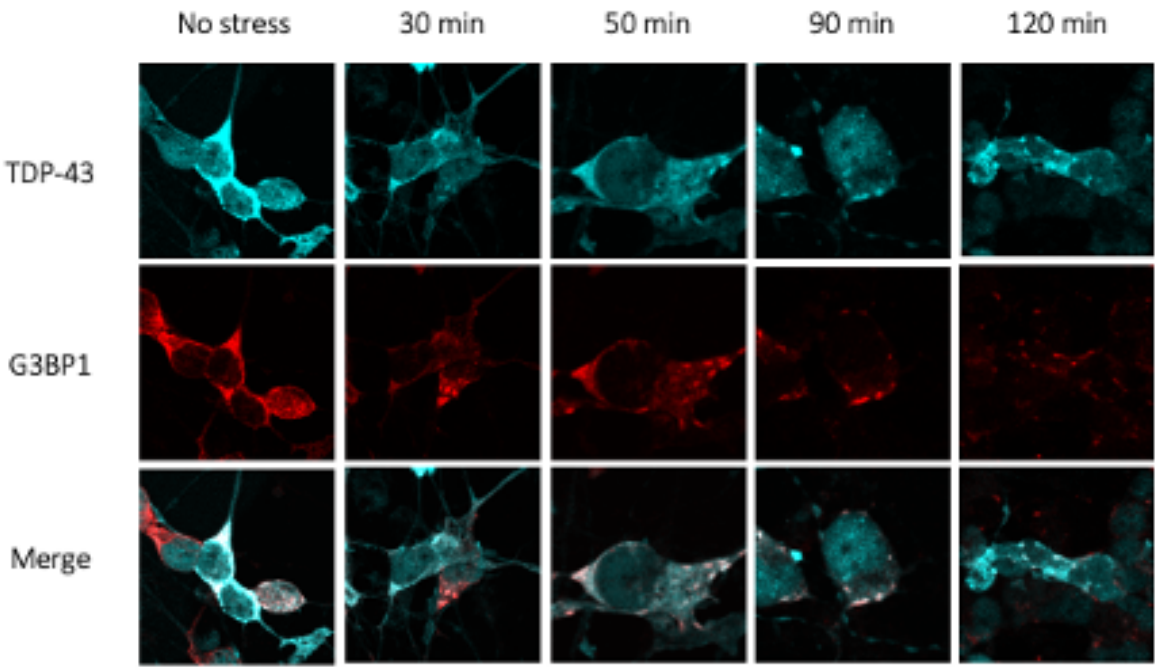

565

566 **Supplementary Figure 3**: Subcellular distribution of TDP-43dNLS under different time points of sodium arsenite
567 stress. Immunostaining of neurons expressing TDP-43dNLS-V5-APEX in different time points after sodium arsenite
568 addition.

569

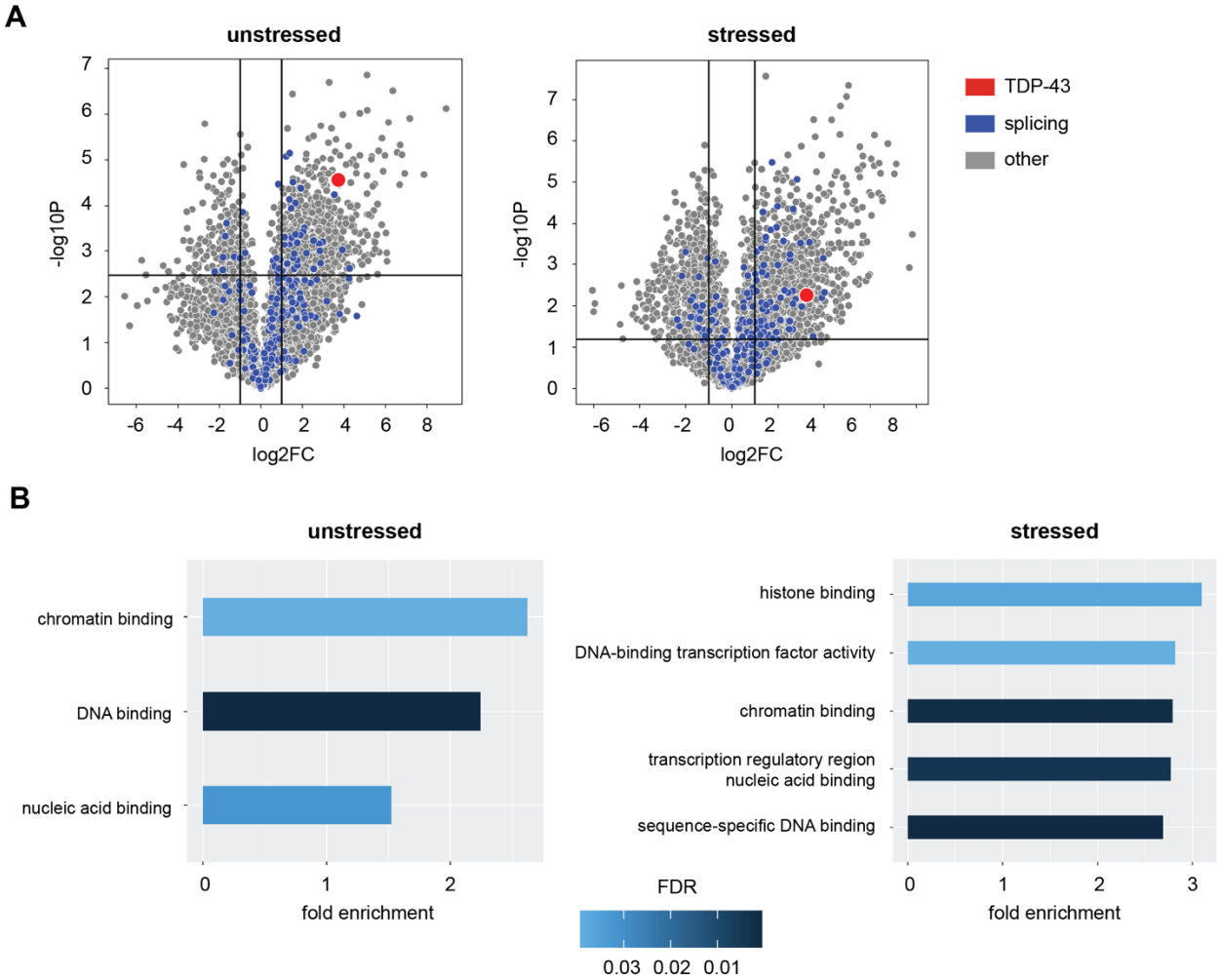

570
571
572 **Supplementary Figure 4: Proximity labeling proteomics to map protein interactors of TDP-43^{deltaNLS}. (A)** Volcano
573 plots of differential protein enrichment in TDP-43^{deltaNLS} samples versus NES samples, without (left) or with (right)
574 addition of sodium arsenite stress. TDP-43 is shown in red and factors associated with the Gene Ontology term
575 'splicing' in blue. **(B)** Gene ontology [173,174] molecular function analysis of proteins enriched in TDP-43^{deltaNLS} samples
576 versus NES samples.
577
578
579

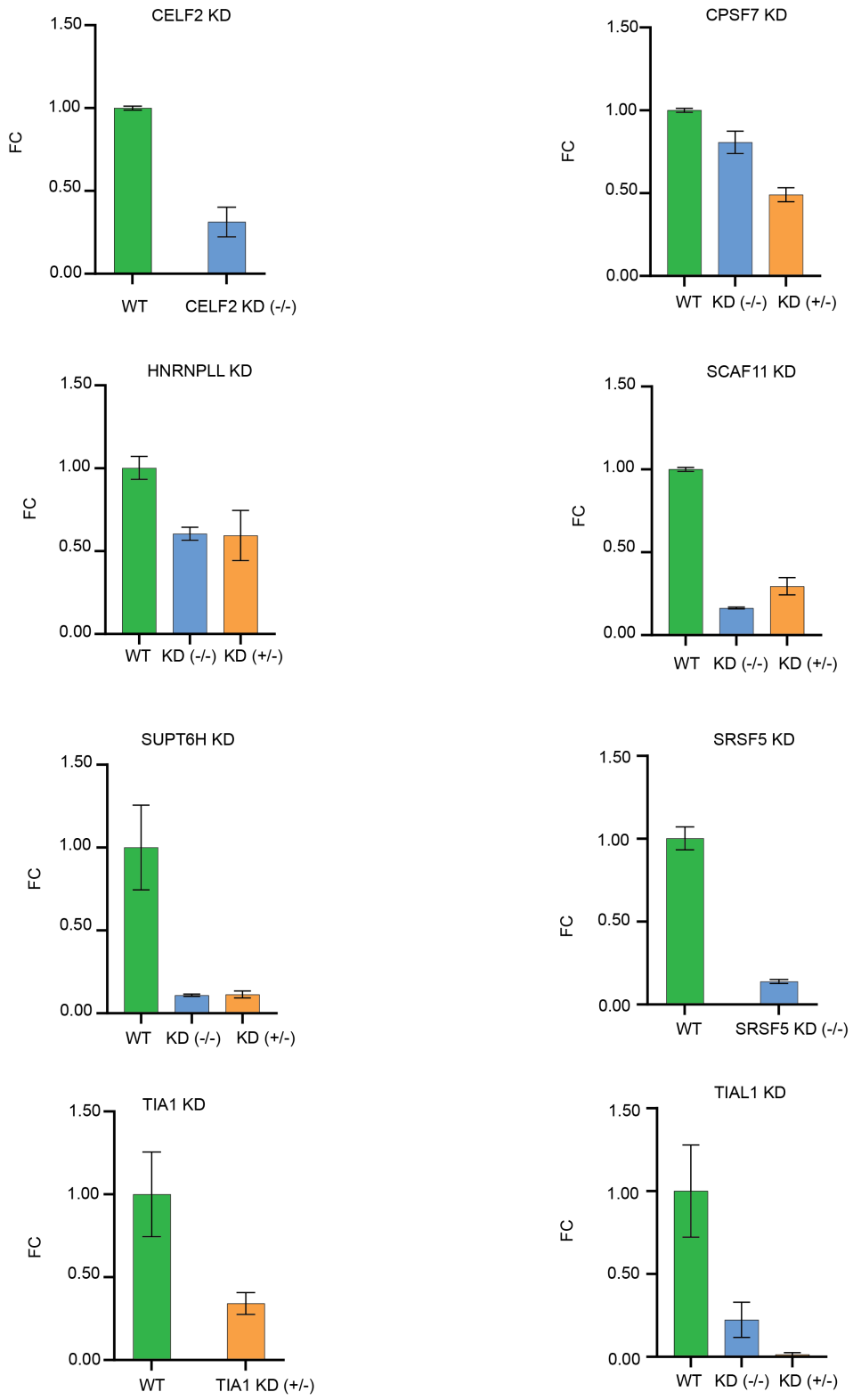

Supplementary Figure 5: Validation of RBP knockdown by qPCR. Relative RNA fold change (FC) in knockdown (KD) iPSCs compared to control.

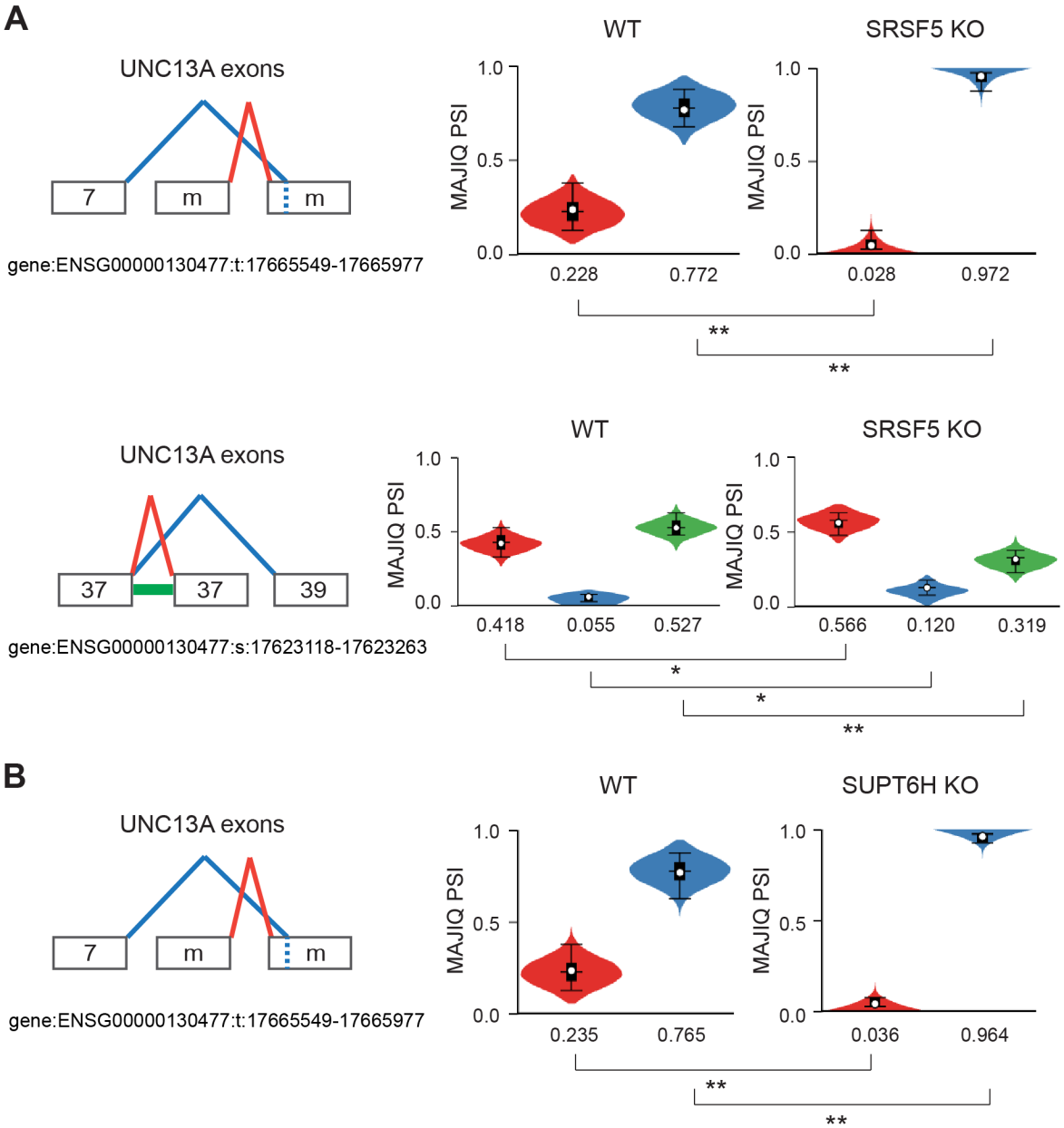

Supplementary Figure 6: Alternative splicing of UNC13A upon SRSF5 and SUPT6H knockdown. (A) Output of MAJIQ deltaPSI analysis comparing WT and **(A)** SRSF5 or **(B)** SUPT6H KD neurons, displaying the two events in UNC13A that were significantly altered. Numbers indicate canonically annotated exons, and 'm' represents exons identified by MAJIQ. P-values: * < 0.1, ** < 0.05.

Materials and methods

Published AD and ALS/FTLD-TDP datasets

For analysis of AD and control brain tissues with and without TDP-43 pathology, we included bulk RNA-seq data from dorsolateral prefrontal cortex (DLPFC) samples from the Religious Orders Study and Rush Memory and Aging Project (ROSMAP) [43] available in Synapse (syn3388564). All participants in ROSMAP were enrolled without known dementia and agreed to annual clinical evaluation and brain donation. Both studies were approved by an Institutional Review Board of Rush University Medical Center. Each participant signed informed and repository consents and an Anatomic Gift Act. Raw bam files (syn4164376) from 300 samples (150 with and 150 without TDP-43 pathology, to approximate the real distribution in patients [19,20]) were used as input for splicing analysis described below. Normalized isoform-level expression data (syn3505746) as determined by RSEM [53] from 505 samples was used as orthogonal verification. When comparing samples without TDP-43 pathology to those with TDP-43 pathology, TDP-43 stage (tdp_st4) was dichotomized as per RADC recommendation: no pathology = no TDP-43 pathology or TDP-43 pathology in amygdala only (Stages 0 and 1); TDP-43 pathology = TDP-43 pathology extending beyond amygdala (Stages 2 and 3) [145,146]. To compare the expression of APP isoforms, we applied a min–max normalization, which scales expression values so that each isoform's minimum and maximum levels correspond to 0 and 1, respectively. We then compared each isoform (APP695, APP751, APP770) individually as well as the sum of the pathogenic isoforms (APP751 + APP770) relative to the canonical APP695 isoform. For measurements of Aβ pathology, we used the RADC amylsqrt_est_8reg variable, reflecting mean amyloid score across 8 brain regions [55,56].

Table 4: Demographics of ROSMAP subjects included in the various splicing analyses.

RSEM	Mean age at death	%Female	Mean education	% AD dementia	Total
No TDP	86	62	16.53	30.7	352
TDP	88	69.2	16.44	49.7	153
MAJIQ	**Mean age at death**	**%Female**	**Mean education**	**% TDP Pathology**	**Total**
control	86	61.6	16.37	15	201
MAJIQ	**Mean age at death**	**%Female**	**Mean education**	**% AD dementia**	**Total**
No TDP	87	58.6	16.8	29.3	150
TDP	91	68.6	16.4	49.3	150

617 Proteomic data of ROSMAP DLPFC tissues was generated as in [57,147].
618
619 For analysis of human autopsy brain tissues from ALS/FTLD-TDP patients, we used existing RNA-seq data
620 as published in [54]. Briefly, nuclei from mid-frontal neocortical brain tissue from 7 patients diagnosed with
621 FTLD-TDP (all carrying C9orf72 hexanucleotide repeat expansions) were isolated and stained for DAPI,
622 NeuN and TDP-43. Using flow cytometry, nuclei with pathological loss of TDP-43 were separated from
623 TDP-43-positive nuclei. Sorted nuclei were then subjected to RNA extraction and Illumina sequencing as
624 described [54].
625
626 **Human iPSC culture**
627 Human iPSCs were grown in mTeSR1 (STEMCELL Technologies, 85850) or mTeSR Plus (STEMCELL
628 Technologies, 100-0276) medium at 37°C with 5% CO2 on tissue culture dishes coated with Geltrex
629 (A1413302, Gibco) or Corning Matrigel (Sigma-Aldrich, CLS354277). Coating was done overnight or for at
630 least 1 hour at 37°C. Cell culture medium was exchanged daily (mTeSR1) or every two days (mTeSR Plus).
631 When reaching ~80% confluency, iPSCs were dissociated with accutase (ThermoFisher Scientific,
632 A1110501) and plated in mTeSR1 containing ROCK inhibitor Y-27632 (10 µM, Tocris Bioscience, 1254). For
633 freezing, cells were resuspended in mTeSR1 supplemented with 30% KnockOut Serum Replacement
634 (ThermoFisher Scientific, 1082802) and 10% DMSO.
635
636 **Generation of knockdown iPSC lines**
637 KOLF2.1J human iPSCs [148] were genetically edited with a BE3 cytidine base editor [111] as described
638 previously [149] with minor adjustments. Guide RNAs were designed with the CRISPR design tool in Benchling
639 to generate premature stop codons and cloned into the pKLV2 gRNA plasmid (Addgene plasmid #67974)
640 using Gibson assembly (NEB). DNA sequences of all guides and primers used for amplifying and sequencing
641 the target region are listed in **Supplementary Table 6**. For each gene target, the top off-target site was
642 amplified and sequenced to verify the absence of off-target edits (see **Supplementary Table 6** for primer
643 sequences). For transfection, 0.5 million iPSCs were seeded into a well of a 6-well plate. The next day,
644 medium was replaced with mTeSR1 supplemented with Rock inhibitor (10 µM). Per reaction, 1 µg of iBE3
645 CLYBL base editor plasmid (Addgene plasmid #174569) and 1 µg of guide plasmid were introduced with
646 TransfeX as described above. Cells were then incubated at 37°C with 5% CO_2 for 24 hours. The two days
647 after transfection, medium was replaced with medium containing puromycin (0.8 µg/ml) and doxycycline
648 (2 µg/ml) each day. On the third day post-transfection, cells were dissociated and seeded into a matrigel-

649 coated 96-well plate at a concentration of 1 cell per well through serial dilution. Cells were grown for ~2
650 weeks as described above until wells were full, with daily medium replacements with Rock inhibitor for
651 the first 2-3 days. After this, medium was replaced once every two days with mTeSR1 without Rock
652 inhibitor. When wells were confluent, single-cell colonies were transferred to a 24-well plate and grown
653 until confluent. Cells were then dissociated and a small amount of cell suspension was harvested in
654 ultrapure water for DNA sequencing before freezing the rest. Positive clones were expanded and the PG-
655 TO-hNGN2 plasmid was integrated into the genome as described above.
656
657 **Differentiation of iPSCs to day 8 neurons**
658 Differentiation was performed as described previously [98] with minor adjustments. Briefly, iPSCs were
659 cultured as detailed above and upon reaching 70%-80% confluency, cells were transferred to geltrex- or
660 matrigel-coated plates for differentiation. Cells were seeded in induction medium containing DMEM/F12
661 HEPES (Gibco, 11330032), N2 supplement (Gibco, 17502048), NEAA (Gibco, 11140050) and L-glutamine
662 (Gibco, 25030081), supplemented with ROCK inhibitor (Tocris Bioscience, 1254, 10 µM) and freshly
663 prepared doxycycline (DOX) solution (2 µg/ml, Sigma-Aldrich D9891). Based on plate size, either 1.5
664 million or 2.5 million iPSCs were seeded in a 10 or 15 cm dish respectively. Induction medium was replaced
665 daily with induction medium containing DOX for three days. On day 2, plates were coated with PDL (Sigma-
666 Aldrich P7405, 0.04mg/ml) overnight. On day 3, plates were washed twice with ultrapure water and dried
667 completely before seeding day 3 neurons per well in maturation medium containing BrainPhys (STEMCELL
668 Technologies, 05790), B27 supplement (Gibco, 17504044), BDNF (PeproTech, 450-02), NT3 (PeproTech,
669 450-03), Laminin (Gibco, 23017-015) and 40mM BrdU (Sigma-Aldrich, B9285). Neurons were matured
670 with half-medium replacements without BrdU every 2-3 days.
671
672 **RNA-seq and splicing analysis**
673 RNA was extracted using the miRNeasy Kit (Qiagen) according to the manufacturer's protocol before
674 measuring RNA concentration with a Nanodrop spectrophotometer. RNA-seq libraries were prepared at
675 the Crown Genomics institute of the Nancy and Stephen Grand Israel National Center for Personalized
676 Medicine, Weizmann Institute of Science. Libraries were prepared using the TruSeq Stranded mRNA-seq
677 kit (Illumina) according to the manufacturing protocol. Briefly, the polyA fraction (mRNA) was purified
678 from 500 ng of total input RNA followed by fragmentation and the generation of double-stranded cDNA.
679 After Agencourt Ampure XP beads cleanup (Beckman Coulter), A base addition, adapter ligation and PCR
680 amplification steps were performed. Libraries were quantified by Qubit (Thermo fisher scientific) and

681 TapeStation (Agilent). Sequencing was done on Novaseq 6000 S1 300 cycles kit or Novaseq X 1.5B 300
682 cycles kit, allocating ~50-60M reads per sample (Illumina; paired end sequencing). In the case of TDP-
683 43^{deltaNLS} and NES samples, sequencing was done with NextSeq high output kit, 75 cycles, allocating ~20M
684 reads per sample (Illumina; single-end sequencing).
685
686 Poly-A/T stretches and Illumina adapters were trimmed from RNA sequencing reads using cutadapt [150];
687 resulting reads shorter than 30bp were discarded. Reads - both those experimentally generated and those
688 from published datasets [10,54,58] - were mapped to the H. sapiens reference genome GRCh38 using STAR [151],
689 supplied with gene annotations downloaded from Ensembl (and with EndToEnd option and
690 outFilterMismatchNoverLmax was set to 0.04). Reads with the same UMI were removed using the PICARD
691 MarkDuplicate tool using the BARCODE_TAG parameter. Pipeline was run using snakemake [152].
692
693 Aligned BAMs were used as input for differential splicing analysis with MAJIQ (v2.5.7) [45] using reference
694 genome GRCh38. A deltaPSI threshold of 2% and probability changing threshold of 0.9 was used to
695 calculate the probability of splicing changes between groups. The RNAseq of RBP KD lines was done in
696 several batches (each time including the control line), so for visualization of APP splice events in **Figure**
697 **5D**, MAJIQ PSI values were normalized against the corresponding control. For analysis of ROSMAP data,
698 the MAJIQ heterogen function was used to compare between groups and a P-value threshold of 0.05 was
699 maintained. The voila tsv output tables were parsed using an adjusted version of the R script from [10] (see
700 Code Availability) to obtain values per junction instead of per junction cluster. P-values of deltaPSI
701 analyses were calculated as *1 - probability changing*.
702
703 **Cellular fractionation**
704 Monoclonal iPSC lines carrying APEX constructs mentioned above were differentiated into cortical
705 neurons as described previously. After 5 days of maturation, construct expression was induced for 24 and
706 4 hours respectively to achieve comparable levels of expression. Cells were washed with PBS once before
707 scraping in lysis buffer A (10 mM Tris Cl, pH 7.5; 10 mM NaCl; 3 mM MgCl2; 0.5% NP40) supplemented
708 with cOmplete Protease Inhibitor Cocktail (Roche, 4693116001) and PhosSTOP (Roche, 4906837001).
709 Lysates were incubated on ice for 10 min while vortexing every few minutes, followed by centrifugation
710 for 10 min at 4°C at maximum speed to precipitate nuclei. After transferring the supernatant (the
711 cytoplasmic fraction) to a new tube, nuclei pellets were repeatedly washed with lysis buffer A via
712 centrifugation for 10 min at 4°C at maximum speed until resuspension was impossible. RIPA buffer (150

713 mM NaCl; 1% NP40; 0.5% deoxycholate (DOC); 0.1% SDS and 50 mM Tris, pH 8) was added to nuclei pellets
714 before sonication for 3 cycles x 10 sec with 20 sec intervals, using 30-40% power. Samples were
715 centrifuged for 10 min at 4°C at maximum speed to gain nuclear fractions (the supernatant).
716
717 **Sample preparation for proteomic analysis**
718 Nuclear and cytoplasmic fractions were subjected to in-solution tryptic digestion using the suspension
719 trapping (S-trap) method as previously described [153]. Briefly, fraction lysates were incubated at 96°C for 5
720 min, followed by six cycles of 30 s of sonication (Bioruptor Pico, Diagenode, USA). Protein concentration
721 was measured using the BCA assay (Thermo Scientific, USA). From each sample 20ug of total protein were
722 reduced with 5 mM dithiothreitol and alkylated with 10 mM iodoacetamide in the dark. Each sample was
723 loaded onto S-Trap microcolumns (Protifi, USA) according to the manufacturer's instructions. After
724 loading, samples were washed with 90:10% methanol/50 mM ammonium bicarbonate. Samples were
725 then digested with trypsin (1:50 trypsin:protein ratio) for 1.5 h at 47°C. The digested peptides were eluted
726 using 50 mM ammonium bicarbonate. Trypsin (1:50 trypsin:protein ratio) was added to this fraction and
727 incubated overnight at 37°C. Two more elutions were made using 0.2% formic acid and 0.2% formic acid
728 in 50% acetonitrile. The three elutions were pooled together and vacuum-centrifuged to dryness. Samples
729 were resuspended in H2O with 0.1% formic acid and subjected to solid phase extraction (Oasis HLB,
730 Waters, Milford, MA, USA) according to manufacturer instructions and vacuum-centrifuged to dryness.
731 Samples were kept at−80°C until further analysis.
732
733 **Liquid chromatography and mass spectrometry**
734 ULC/MS grade solvents were used for all chromatographic steps. Dry digested samples were dissolved in
735 97:3% H2O/acetonitrile + 0.1% formic acid. Each sample was loaded using split-less nano-Ultra
736 Performance Liquid Chromatography (10 kpsi nanoAcquity; Waters, Milford, MA, USA). The mobile phase
737 was: A) H2O + 0.1% formic acid and B) acetonitrile + 0.1% formic acid. Desalting of the samples was
738 performed online using a reversed-phase Symmetry C18 trapping column (180 µm internal diameter, 20
739 mm length, 5 µm particle size; Waters). The peptides were then separated using a T3 HSS nano-column
740 (75 µm internal diameter, 250 mm length, 1.8 µm particle size; Waters) at 0.35 µL/min. Peptides were
741 eluted from the column into the mass spectrometer using the following gradient: 4% to 30%B in 105 min,
742 30% to 90%B in 10 min, maintained at 90% for 7 min and then back to initial conditions.
743

744 The nanoUPLC was coupled online through a nanoESI emitter (10 µm tip; New Objective; Woburn, MA,
745 USA) to a quadrupole orbitrap mass spectrometer (Exploris 480, Thermo Scientific) using a FlexIon
746 nanospray apparatus (Proxeon). Data was acquired in data dependent acquisition (DDA) mode, using a 2-
747 seconds cycle time method. MS1 resolution was set to 120,000 (at 200m/z), mass range of 380-1500m/z,
748 AGC of 200% and maximum injection time was set to 50msec. MS2 resolution was set to 15,000,
749 quadrupole isolation 1.4m/z, AGC set to custom, dynamic exclusion of 40sec and maximum injection time
750 set to auto.
751
752 **Raw proteomic data analysis**
753 Raw data was analyzed using MaxQuant (v1.6.6.0) [154]. The data was searched with the Andromeda search
754 engine against the human (Homo sapiens) protein databases as downloaded from Uniprot
755 (www.uniprot.com), appended with common lab protein contaminants. Enzyme specificity was set to
756 trypsin and up to two missed cleavages were allowed. Fixed modification was set to
757 carbamidomethylation of cysteines. Variable modifications were set to oxidation of methionines, and
758 protein N-terminal acetylation. Peptide precursor ions were searched with a maximum mass deviation of
759 4.5 ppm and fragment ions with a maximum mass deviation of 20 ppm. Peptide and protein identifications
760 were filtered at an FDR of 1% using the decoy database strategy (MaxQuant's "Revert" module). The
761 minimal peptide length was 7 amino-acids and the minimum Andromeda score for modified peptides was
762 40. Peptide identifications were propagated across samples using the match-between-runs option
763 checked. Searches were performed with the label-free quantification option selected.
764
765 **Proteomics statistical analysis**
766 MaxQuant output table ProteinGroups was imported to Perseus and analyzed as follows. Reverse
767 proteins, proteins identified only based on a modified peptide and contaminants were excluded before
768 log2-transforming the data. Rows were filtered to keep only those with at least 6 valid values, and missing
769 values were replaced by low values from a normal distribution. Two-sample t-test comparing samples
770 with biotin to samples without biotin was performed to remove non-specific binders (FDR < 0.05, log2FC
771 > 0). Samples were separated based on stress condition before filtering to remain only those proteins with
772 a minimum of 2 valid values in at least one experimental group (TDP-43^{deltaNLS} or NES). Missing values were
773 imputed again using a normal distribution. Two-sample t-test using log2-transformed LFQ values was
774 performed to gain proteins enriched in TDP-43^{deltaNLS}.
775

776 **RNA Extraction and cDNA Synthesis**

777 RNA was extracted from day 8 differentiated cells using the miRNeasy MicroKit (Qiagen) according to the
778 manufacturer's protocol. The RNA concentration was measured using a Nanodrop spectrophotometer,
779 and 500 ng of RNA was used for reverse transcription. First-strand cDNA synthesis was performed using
780 the High-Capacity cDNA Reverse Transcription Kit (Thermo, catalog number 4368814) in accordance with
781 the respective manufacturer's instructions.

782 **RT-PCR**

783 PCR amplification was carried out using the RedTaq Ready Mix PCR Reaction Mix (Sigma-Aldrich, catalog
784 number R2523), which contains RedTaq DNA polymerase, dNTPs, buffer, and magnesium chloride in a
785 pre-mixed, ready-to-use format. The PCR reaction was prepared by combining the following components:
786 1X final concentration of RedTaq Ready Mix, gene-specific forward and reverse primers, cDNA template,
787 and nuclease-free water to a final reaction volume. For amplification of APP770 specifically, the following
788 primers were used: CCCATTCTTTTACGGCGGATG and AACAGGATCTCGGGCAAGAGG. To amplify the region
789 between exons 6 and 9, primers TCTGTGGAAGAGGTGGTTCG and GGCCTCAAGCCTCTCTTTGG were used.
790 PCR amplification was performed under the following conditions: initial denaturation at 95°C for 5
791 minutes, followed by 28 cycles of denaturation at 95°C for 30 seconds, primer-specific annealing at the
792 appropriate temperature for 30 seconds, and extension at 72°C for 1 minute. A final extension step was
793 performed at 72°C for 5 minutes. Following amplification, PCR products were analyzed by agarose gel
794 electrophoresis using a 1.8% agarose gel. The PCR products were loaded onto the gel, and electrophoresis
795 was carried out at 120V for approximately 1 hour. The bands were visualized under UV light to confirm
796 the presence and size of the amplified products.

797 **Immunofluorescence and imaging**

798 Differentiation of iPSCs into cortical neurons was done as described above; on day 3, approximately
799 60,000 neurons were seeded per well of a 96-well plate (Brooks, MGB096-1-2-LG-L). Neurons were fixed
800 on day 8 in 4% PFA in 1X PBS++ for approximately 15 minutes. After one wash with PBS, cells were
801 incubated in 0.1% TritonX in PBS for permeabilization for 10-15 minutes followed by blocking with
802 CasBlock reagent for 10 minutes at room temperature (RT). Primary antibodies (purified anti-β-Amyloid
803 1-16 Antibody, BioLegend 803004; Thioflavine S, Sigma-Aldrich T1892; anti-Amyloid Precursor Protein,
804 Sigma-Aldrich A8717) were diluted in CasBlock and 75 µl of this mix was added to each well for overnight
805 incubation at 4°C. The next day, cells were washed in PBS twice for 5 minutes. Anti-mouse Cy5 secondary

806 antibody (Jackson ImmunoResearch 715-175-150) was diluted in PBS before incubation with 75 µl per well
807 for 1 hour at RT in the dark. For DNA staining, Hoechst (ThermoFisher 62249, diluted 1:8000 in PBS) was
808 added to the cells after one PBS wash for 10-30 minutes at RT. The Hoechst solution was replaced with
809 PBS before proceeding with imaging. Confocal images were acquired on the Opera Phenix Plus High-
810 Content Imaging System.
811
812 **Image quantification**
813 A specific CellProfiler (version 4.2.1) [155,156] pipeline was built for quantification of beta-amyloid and
814 thioflavin intensity. First, nuclei were detected with IdentifyPrimaryObject and used as input for
815 Secondary Object identification using the Thioflavin S signal, which was distributed throughout the entire
816 cell. The cytoplasm was demarcated with IdentifyTertiaryObjects by subtracting the nucleus from the
817 Thioflavin S signal. Amyloid and Thioflavin S intensity were measured in the cytoplasm and averaged
818 across cells per image before plotting and statistical testing in Prism (version 10).
819 Quantification of puncta was performed using Harmony (version 5.2). Nuclei were segmented from the
820 Hoechst channel using the "Find Nuclei" building block, with parameters optimized to accurately detect
821 individual nuclei. The cytoplasm was then delineated using the "Find Cytoplasm" building block, which
822 expanded outward from the nuclear boundary by utilizing the Cy3 channel, which detects amyloid
823 precursor protein (APP), to generate a whole-cell mask.
824 Beta-amyloid and/or Thioflavin S puncta were identified using the "Find Spots" building block in the
825 respective channels. Spot detection parameters, including spot size range and intensity thresholds, were
826 optimized to capture distinct punctate structures while minimizing background noise. For puncta analysis,
827 point intensities were measured on a per-spot basis. The output data, including total puncta count and
828 the number of cells, were exported from Harmony. The number of puncta was then normalized to the
829 number of cells, providing a puncta-to-cell ratio for each field of view.
830
831 **Mediation analysis**
832 Mediation analysis was conducted to examine whether APP mediates the relationship between TDP-43
833 pathology and amyloid-β pathology. When modeling different isoforms of APP into a single ratio variable
834 (e.g., APP571+APP7701+APP695), each APP isoform underwent min-max scaling before computing the
835 sum/ratio. The total, direct, and indirect effects were estimated using Ordinary Least Squares (OLS)
836 regression models (**Table 3**). First, we assessed the effect of TDP-43 on APP (path a). Next, we examined
837 the effect of APP on amyloid-β while controlling for TDP-43 (path b). The total effect (c) of TDP-43 on

amyloid-β was decomposed into the direct effect (c', TDP-43's effect on amyloid-β independent of APP) and the indirect effect (a × b), representing mediation. To test the statistical significance of the indirect effect, we used bias-corrected bootstrap confidence intervals (95% CI) with n = 1,000 resamples. The proportion of the total effect mediated was computed as abc. All statistical analyses were performed in Python 3.6 using the statsmodels package, and results were considered statistically significant at $p < 0.05$.

Code availability

Code for running MAJIQ and plotting the results can be found on our Github page:
https://github.com/WelmoedVZ/splicing.git

Data availability

Proximity labeling proteomics data have been deposited to the ProteomeXchange Consortium via the PRIDE [157] partner repository with the dataset identifier PXD063021.

Reviewer access details: Log in to the PRIDE website using the following details:

Project accession: PXD063021

Token: D4CuJoBtiplr

Alternatively, reviewer can access the dataset by logging in to the PRIDE website using the following account details:

Username: reviewer_pxd063021@ebi.ac.uk

Password: mWEo5AKvWcaS

Similarly, fractionation mass spectrometry data is available in ProteomeXchange under PXD063188. Reviewer access details: Log in to the PRIDE website using the following details:

Project accession: PXD063188

Token: CIWLhWEMDidP

Alternatively, reviewer can access the dataset by logging in to the PRIDE website using the following account details:

Username: reviewer_pxd063188@ebi.ac.uk

Password: Rmq1hfujAb4N

Raw RNA-seq data are available in Sequence Read Archive under accession number PRJNA1255884.

Acknowledgements

We wish to thank Michael Ward (NINDS, NIH) and Bill Skarnes (Jackson labs) for access to iPSC lines. We thank Alon Savidor (WIS) and Yishai Levin (WIS) for mass spectrometry, and Inbal Bolocan Nachman (WIS) and Yuval Elazari (WIS) for RNA sequencing. We also thank Noa Wigoda (WIS), Melina Klostermann (Julius-Maximilians-Universität Würzburg) and the BioCiphers team for bioinformatics advice. To Prof. Naomi Habib and Anael Cain (HUJI) we are grateful for advice and discussions. We thank Anna-Leigh Brown (UCL), Jack Humphrey (MSSM) and Pietro Fratta (UCL) for advice on splicing.

EH is the Mondry Family Professorial Chair and Head of the Andrea L. and Lawrence A. Wolfe Family Center for Research on Neuroimmunology and Neuromodulation. Funding for research: Binational Science Foundation (BSF); Association Francaise Contre les Myopathies (AFM); Amyotrophic Lateral Sclerosis Association (ALSA); Target ALS; Israel Science Foundation (ISF 3497/21, 424/22, 494/24); ALS Canada; Minna-James-Heineman Stiftung through Minerva, Minerva Foundation, with funding from the Federal German Ministry for Education and Research; Robert Packard Center for ALS Research at Johns Hopkins; McGill University; EU - ERA-Net; Radala Foundation for ALS Research; Additional support generously provided by the Kekst Family Institute for Medical Genetics. Weizmann SABRA - Yeda-Sela - WRC Program, the Estate of Emile Mimran, and The Maurice and Vivienne Wohl Biology Endowment. Nella and Leon Benoziyo Center for Neurological Diseases. Goldhirsh-Yellin Foundation. Dr. Sydney Brenner and friends. Weizmann - Center for Research on Neurodegeneration. Redhill Foundation – Sam and Jean Rothberg Charitable Trust Dr. Dvora and Haim Teitelbaum Endowment Fund. LM is funded by a Minerva Postdoctoral Fellowship. YDM is funded by the Weizmann - CNRS (Centre National de la Recherche Scientifique) Collaboration Program.

ROSMAP is supported by P30AG10161, P30AG72975, R01AG15819, R01AG17917, U01AG46152, and U01AG61356. ROSMAP resources can be requested at https://www.radc.rush.edu and www.synpase.org.

900 **References**

901 1. Nikom, D. & Zheng, S. Alternative splicing in neurodegenerative disease and the promise of RNA
902 therapies. *Nat. Rev. Neurosci.* **24**, 457–473 (2023).
903 2. Sattler, R. & Donnelly, C. J. *RNA Metabolism in Neurodegenerative Diseases*. (Springer, 2018).
904 3. Birsa, N., Bentham, M. P. & Fratta, P. Cytoplasmic functions of TDP-43 and FUS and their role in
905 ALS. *Seminars in Cell and Developmental Biology* vol. 99 193–201 Preprint at
906 https://doi.org/10.1016/j.semcdb.2019.05.023 (3 2020).
907 4. Ratti, A. & Buratti, E. Physiological functions and pathobiology of TDP-43 and FUS/TLS proteins.
908 *Journal of Neurochemistry* vol. 138 Suppl 95–111 Preprint at https://doi.org/10.1111/jnc.13625 (8 2016).
909 5. Neumann, M. *et al.* Ubiquitinated TDP-43 in frontotemporal lobar degeneration and
910 amyotrophic lateral sclerosis. *Science* **314**, 130–133 (10 2006).
911 6. Suk, T. R. & Rousseaux, M. W. C. The role of TDP-43 mislocalization in amyotrophic lateral
912 sclerosis. *Mol. Neurodegener.* **15**, (8 2020).
913 7. Arai, T. *et al.* TDP-43 is a component of ubiquitin-positive tau-negative inclusions in
914 frontotemporal lobar degeneration and amyotrophic lateral sclerosis. *Biochem. Biophys. Res. Commun.*
915 **351**, 602–611 (2006).
916 8. Mackenzie, I. R. A. *et al.* Pathological TDP-43 distinguishes sporadic amyotrophic lateral sclerosis
917 from amyotrophic lateral sclerosis with SOD1 mutations. *Ann. Neurol.* **61**, 427–434 (2007).
918 9. Ma, X. R. *et al.* TDP-43 represses cryptic exon inclusion in the FTD-ALS gene UNC13A. *Nature*
919 **603**, 124–130 (2022).
920 10. Brown, A.-L. *et al.* TDP-43 loss and ALS-risk SNPs drive mis-splicing and depletion of UNC13A.
921 *Nature* **603**, 131–137 (2022).
922 11. Klim, J. R. *et al.* ALS-implicated protein TDP-43 sustains levels of STMN2, a mediator of motor
923 neuron growth and repair. *Nat. Neurosci.* **22**, 167–179 (2019).
924 12. Ling, J. P., Pletnikova, O., Troncoso, J. C. & Wong, P. C. TDP-43 repression of nonconserved
925 cryptic exons is compromised in ALS-FTD. *Science* **349**, 650–655 (2015).
926 13. Melamed, Z. ’ev *et al.* Premature polyadenylation-mediated loss of stathmin-2 is a hallmark of
927 TDP-43-dependent neurodegeneration. *Nat. Neurosci.* **22**, 180–190 (2019).
928 14. Prudencio, M. *et al.* Truncated stathmin-2 is a marker of TDP-43 pathology in frontotemporal
929 dementia. *J. Clin. Invest.* **130**, 6080–6092 (2020).
930 15. Agra Almeida Quadros, A. R. *et al.* Cryptic splicing of stathmin-2 and UNC13A mRNAs is a
931 pathological hallmark of TDP-43-associated Alzheimer’s disease. *Acta Neuropathol.* **147**, 9 (2024).

932 16. Nguyen, T. B. *et al.* Aberrant splicing in Huntington's disease accompanies disrupted TDP-43
933 activity and altered m6A RNA modification. *Nat Neurosci* **28**, 280–292 (2025).
934 17. Sun, M. *et al.* Cryptic exon incorporation occurs in Alzheimer's brain lacking TDP-43 inclusion but
935 exhibiting nuclear clearance of TDP-43. *Acta Neuropathol.* **133**, 923–931 (2017).
936 18. Estades Ayuso, V. *et al.* TDP-43-regulated cryptic RNAs accumulate in Alzheimer's disease brains.
937 *Mol Neurodegener* **18**, 57 (2023).
938 19. Arai, T. *et al.* Phosphorylated TDP-43 in Alzheimer's disease and dementia with Lewy bodies.
939 *Acta Neuropathol.* **117**, 125–136 (2009).
940 20. Meneses, A. *et al.* TDP-43 Pathology in Alzheimer's Disease. *Mol. Neurodegener.* **16**, (12 2021).
941 21. Tomé, S. O. *et al.* TDP-43 pathology is associated with increased tau burdens and seeding. *Mol.*
942 *Neurodegener.* **18**, 71 (2023).
943 22. Raj, T. *et al.* Integrative transcriptome analyses of the aging brain implicate altered splicing in
944 Alzheimer's disease susceptibility. *Nat. Genet.* **50**, 1584–1592 (11 2018).
945 23. Kim, S., Han, S., Nho, K., Lee, Y. & Koh, I. Brain regional alternative splicing and clinical traits in
946 Alzheimer's disease. *Alzheimers. Dement.* **19**, e068340 (2023).
947 24. Love, J. E., Hayden, E. J. & Rohn, T. T. Alternative splicing in Alzheimer's disease. *J. Parkinsons*
948 *Dis. Alzheimers Dis.* **2**, 6 (2015).
949 25. Adusumalli, S., Ngian, Z.-K., Lin, W.-Q., Benoukraf, T. & Ong, C.-T. Increased intron retention is a
950 post-transcriptional signature associated with progressive aging and Alzheimer's disease. *Aging Cell* **18**,
951 e12928 (2019).
952 26. Braggin, J. E. *et al.* Alternative splicing in a presenilin 2 variant associated with Alzheimer
953 disease. *Ann. Clin. Transl. Neurol.* **6**, 762–777 (2019).
954 27. Han, S. *et al.* Identification of exon skipping events associated with Alzheimer's disease in the
955 human hippocampus. *BMC Med. Genomics* **12**, 13 (2019).
956 28. Lee, Y. *et al.* Genetic variation affecting exon skipping contributes to brain structural atrophy in
957 Alzheimer's disease. *AMIA Summits Transl. Sci. Proc.* **2017**, 124–131 (2018).
958 29. O'Brien, R. J. & Wong, P. C. Amyloid precursor protein processing and Alzheimer's disease.
959 *Annual review of neuroscience* vol. 34 185–204 Preprint at https://doi.org/10.1146/ANNUREV-NEURO-
960 061010-113613 (7 2011).
961 30. Orobets, K. S. & Karamyshev, A. L. Amyloid precursor protein and Alzheimer's disease. *Int. J.*
962 *Mol. Sci.* **24**, (2023).

963 31. Yang, L.-B. *et al.* Elevated beta-secretase expression and enzymatic activity detected in sporadic
964 Alzheimer disease. *Nat. Med.* **9**, 3–4 (2003).
965 32. Johnston, J. A. *et al.* Expression and activity of beta-site amyloid precursor protein cleaving
966 enzyme in Alzheimer's disease. *Biochem. Soc. Trans.* **33**, 1096–1100 (2005).
967 33. Lanoiselée, H.-M. *et al.* APP, PSEN1, and PSEN2 mutations in early-onset Alzheimer disease: A
968 genetic screening study of familial and sporadic cases. *PLoS Med.* **14**, e1002270 (2017).
969 34. Andrade-Guerrero, J. *et al.* Alzheimer's disease: An updated overview of its genetics. *Int. J. Mol.*
970 *Sci.* **24**, 3754 (2023).
971 35. Weggen, S. & Beher, D. Molecular consequences of amyloid precursor protein and presenilin
972 mutations causing autosomal-dominant Alzheimer's disease. *Alzheimers. Res. Ther.* **4**, 9 (2012).
973 36. Nalivaeva, N. N. & Turner, A. J. The amyloid precursor protein: a biochemical enigma in brain
974 development, function and disease. *FEBS Lett.* **587**, 2046–2054 (6 2013).
975 37. Sandbrink, R., Masters, C. L. & Beyreuther, K. APP gene family. Alternative splicing generates
976 functionally related isoforms. *Ann. N. Y. Acad. Sci.* **777**, 281–287 (1996).
977 38. Moir, R. D. *et al.* Relative increase in Alzheimer's disease of soluble forms of cerebral Abeta
978 amyloid protein precursor containing the Kunitz protease inhibitory domain. *J. Biol. Chem.* **273**, 5013–
979 5019 (2 1998).
980 39. Urakami, K. *et al.* Amyloid beta protein precursors with kunitz-type inhibitor domains and
981 acetylcholinesterase in cerebrospinal fluid from patients with dementia of the Alzheimer type. *Acta*
982 *Neurol. Scand.* **85**, 343–346 (1992).
983 40. Bordji, K., Becerril-Ortega, J., Nicole, O. & Buisson, A. Activation of extrasynaptic, but not
984 synaptic, NMDA receptors modifies amyloid precursor protein expression pattern and increases
985 amyloid-ß production. *J. Neurosci.* **30**, 15927–15942 (2010).
986 41. Tanaka, S. *et al.* Three types of amyloid protein precursor mRNA in human brain: their
987 differential expression in Alzheimer's disease. *Biochem. Biophys. Res. Commun.* **157**, 472–479 (1988).
988 42. Zhan, S. S., Sandbrink, R., Beyreuther, K. & Schmitt, H. P. APP with Kunitz type protease inhibitor
989 domain (KPI) correlates with neuritic plaque density but not with cortical synaptophysin
990 immunoreactivity in Alzheimer's disease and non-demented aged subjects: a multifactorial analysis. *Clin.*
991 *Neuropathol.* **14**, 142–149 (1995).
992 43. Bennett, D. A. *et al.* Religious Orders Study and Rush Memory and Aging Project. *J. Alzheimers.*
993 *Dis.* **64**, S161–S189 (2018).
994 44. Logsdon, B. ROSMAP RNAseq BAM files. Synapse https://doi.org/10.7303/SYN4164376 (2016).

995 45. Vaquero-Garcia, J. *et al.* A new view of transcriptome complexity and regulation through the
996 lens of local splicing variations. *eLife* vol. 5 Preprint at https://doi.org/10.7554/ELIFE.11752 (2 2016).
997 46. Zeng, F.-F. *et al.* Association of PICALM gene polymorphisms with Alzheimer's disease: Evidence
998 from an updated meta-analysis. *Curr. Alzheimer Res.* **16**, 1196–1205 (2019).
999 47. Chen, K., Gao, T., Bai, Z. & Yuan, Z. Circulating APP, NCAM and Aβ serve as biomarkers for
1000 Alzheimer's disease. *Brain Res.* **1699**, 117–120 (2018).
1001 48. Aisa, B. *et al.* Altered NCAM expression associated with the cholinergic system in Alzheimer's
1002 disease. *J. Alzheimers. Dis.* **20**, 659–668 (2010).
1003 49. Gamir-Morralla, A. *et al.* Kidins220 correlates with tau in Alzheimer's disease brain and
1004 cerebrospinal fluid. *J. Alzheimers. Dis.* **55**, 1327–1333 (2017).
1005 50. Buchholz, S. & Zempel, H. The six brain-specific TAU isoforms and their role in Alzheimer's
1006 disease and related neurodegenerative dementia syndromes. *Alzheimers. Dement.* **20**, 3606–3628
1007 (2024).
1008 51. Oltersdorf, T. *et al.* The secreted form of the Alzheimer's amyloid precursor protein with the
1009 Kunitz domain is protease nexin-II. *Nature* **341**, 144–147 (1989).
1010 52. Kitaguchi, N., Takahashi, Y., Tokushima, Y., Shiojiri, S. & Ito, H. Novel precursor of Alzheimer's
1011 disease amyloid protein shows protease inhibitory activity. *Nature* **331**, 530–532 (1988).
1012 53. Li, B. & Dewey, C. N. RSEM: accurate transcript quantification from RNA-Seq data with or
1013 without a reference genome. *BMC Bioinformatics* **12**, 323 (8 2011).
1014 54. Liu, E. Y. *et al.* Loss of Nuclear TDP-43 Is Associated with Decondensation of LINE
1015 Retrotransposons. *Cell Rep.* **27**, 1409–1421.e6 (2019).
1016 55. Kapasi, A. *et al.* High-throughput digital quantification of Alzheimer disease pathology and
1017 associated infrastructure in large autopsy studies. *J. Neuropathol. Exp. Neurol.* **82**, 976–986 (2023).
1018 56. Variable Details.
1019 https://www.radc.rush.edu/docs/var/detail.htm?category=Pathology&subcategory=Beta-
1020 Amyloid&variable=amylsqrt_est_8reg.
1021 57. Seifar, F. *et al.* Large-scale deep proteomic analysis in Alzheimer's disease brain regions across
1022 race and ethnicity. *Alzheimers. Dement.* **20**, 8878–8897 (2024).
1023 58. Roczniak-Ferguson, A. & Ferguson, S. M. Pleiotropic requirements for human TDP-43 in the
1024 regulation of cell and organelle homeostasis. *Life Sci. Alliance* **2**, e201900358 (2019).
1025 59. Krispin, S. *et al.* Organellomics: AI-driven deep organellar phenotyping reveals novel ALS
1026 mechanisms in human neurons. (2024) doi:10.1101/2024.01.31.572110.

1027 60. Ashburner, M. *et al.* Gene Ontology: tool for the unification of biology. *Nature Genetics 2000*
1028 *25:1* **25**, 25–29 (5 2000).
1029 61. Consortium, T. G. O. *et al.* The Gene Ontology knowledgebase in 2023. *Genetics* **224**, (5 2023).
1030 62. David, G. *et al.* The RNA-binding proteins CELF1 and ELAVL1 cooperatively control the
1031 alternative splicing of CD44. *Biochem. Biophys. Res. Commun.* **626**, 79–84 (2022).
1032 63. Xia, H. *et al.* CELF1 preferentially binds to exon-intron boundary and regulates alternative
1033 splicing in HeLa cells. *Biochim. Biophys. Acta* **1860**, 911–921 (2017).
1034 64. Xiao, J., Jin, S., Wang, X., Huang, J. & Zou, H. CELF1 selectively regulates Alternative Splicing of
1035 DNA repair genes associated with cataract in human lens cell line. *Biochem. Genet.* **61**, 1319–1333
1036 (2023).
1037 65. Millevoi, S. *et al.* An interaction between U2AF 65 and CF I(m) links the splicing and 3' end
1038 processing machineries. *EMBO J.* **25**, 4854–4864 (2006).
1039 66. Bai, R. *et al.* Structure of the activated human minor spliceosome. *Science* **371**, eabg0879 (2021).
1040 67. Dardenne, E. *et al.* RNA helicases DDX5 and DDX17 dynamically orchestrate transcription,
1041 miRNA, and splicing programs in cell differentiation. *Cell Rep.* **7**, 1900–1913 (2014).
1042 68. He, C., Zhang, G., Lu, Y., Zhou, J. & Ren, Z. DDX17 modulates the expression and alternative
1043 splicing of genes involved in apoptosis and proliferation in lung adenocarcinoma cells. *PeerJ* **10**, e13895
1044 (2022).
1045 69. Taylor, K. *et al.* Modulatory role of RNA helicases in MBNL-dependent alternative splicing
1046 regulation. *Cell. Mol. Life Sci.* **80**, 335 (2023).
1047 70. Gencheva, M., Kato, M., Newo, A. N. S. & Lin, R.-J. Contribution of DEAH-box protein DHX16 in
1048 human pre-mRNA splicing. *Biochem. J.* **429**, 25–32 (2010).
1049 71. Weng, M.-T. & Luo, J. The enigmatic ERH protein: its role in cell cycle, RNA splicing and cancer.
1050 *Protein Cell* **4**, 807–812 (2013).
1051 72. Kozlowski, P. Thirty years with ERH: An mRNA splicing and mitosis factor only or rather a novel
1052 genome integrity protector? *Cells* **12**, 2449 (2023).
1053 73. Kroupova, A. *et al.* Molecular architecture of the human tRNA ligase complex. *Elife* **10**, (2021).
1054 74. Oberdoerffer, S. *et al.* Regulation of CD45 alternative splicing by heterogeneous
1055 ribonucleoprotein, hnRNPLL. *Science* **321**, 686–691 (2008).
1056 75. Chang, X., Li, B. & Rao, A. RNA-binding protein hnRNPLL regulates mRNA splicing and stability
1057 during B-cell to plasma-cell differentiation. *Proc. Natl. Acad. Sci. U. S. A.* **112**, E1888–97 (2015).

1058 76. Wang, X. *et al.* hnRNPLL controls pluripotency exit of embryonic stem cells by modulating
1059 alternative splicing of Tbx3 and Bptf. *EMBO J.* **40**, e104729 (2 2021).
1060 77. Chen, X. *et al.* hnRNPLL regulates MYOF alternative splicing and correlates with early metastasis
1061 in pancreatic ductal adenocarcinoma. *Cancer Lett.* **611**, 217436 (2024).
1062 78. Dagher, S. F., Wang, J. L. & Patterson, R. J. Identification of galectin-3 as a factor in pre-mRNA
1063 splicing. *Proc. Natl. Acad. Sci. U. S. A.* **92**, 1213–1217 (1995).
1064 79. Voss, P. G., Haudek, K. C., Patterson, R. J. & Wang, J. L. Galectin-3-U1 snRNP complexes initiate
1065 splicing activity in U1-depleted nuclear extracts. *Methods Mol. Biol.* **2442**, 713–726 (2022).
1066 80. Straub, T. *et al.* The RNA-splicing factor PSF/p54 controls DNA-topoisomerase I activity by a
1067 direct interaction. *J. Biol. Chem.* **273**, 26261–26264 (1998).
1068 81. Fox, A. H. & Lamond, A. I. Paraspeckles. *Cold Spring Harb. Perspect. Biol.* **2**, a000687 (2010).
1069 82. Vuong, J. K. *et al.* PTBP1 and PTBP2 serve both specific and redundant functions in neuronal pre-
1070 mRNA splicing. *Cell Rep.* **17**, 2766–2775 (2016).
1071 83. Rossi, F. *et al.* Involvement of U1 small nuclear ribonucleoproteins (snRNP) in 5' splice site-U1
1072 snRNP interaction. *J. Biol. Chem.* **271**, 23985–23991 (1996).
1073 84. Heinrichs, V., Bach, M., Winkelmann, G. & Lührmann, R. U1-specific protein C needed for
1074 efficient complex formation of U1 snRNP with a 5' splice site. *Science* **247**, 69–72 (1990).
1075 85. Ge, H., Zuo, P. & Manley, J. L. Primary structure of the human splicing factor ASF reveals
1076 similarities with Drosophila regulators. *Cell* **66**, 373–382 (1991).
1077 86. Das, S. & Krainer, A. R. Emerging functions of SRSF1, splicing factor and oncoprotein, in RNA
1078 metabolism and cancer. *Mol. Cancer Res.* **12**, 1195–1204 (2014).
1079 87. Zahler, A. M., Lane, W. S., Stolk, J. A. & Roth, M. B. SR proteins: a conserved family of pre-mRNA
1080 splicing factors. *Genes Dev.* **6**, 837–847 (1992).
1081 88. Long, J. C. & Caceres, J. F. The SR protein family of splicing factors: master regulators of gene
1082 expression. *Biochem. J.* **417**, 15–27 (2009).
1083 89. Fu, X. D. & Maniatis, T. Isolation of a complementary DNA that encodes the mammalian splicing
1084 factor SC35. *Science* **256**, 535–538 (1992).
1085 90. Li, K. & Wang, Z. Splicing factor SRSF2-centric gene regulation. *Int. J. Biol. Sci.* **17**, 1708–1715
1086 (2021).
1087 91. Tan, W., Wang, W. & Ma, Q. Physiological and pathological function of Serine/arginine-rich
1088 splicing factor 4 and related diseases. *Biomed Res. Int.* **2018**, 3819719 (2018).

1089 92. Screaton, G. R. *et al.* Identification and characterization of three members of the human SR
1090 family of pre-mRNA splicing factors. *EMBO J.* **14**, 4336–4349 (1995).
1091 93. Yang, S., Jia, R. & Bian, Z. SRSF5 functions as a novel oncogenic splicing factor and is upregulated
1092 by oncogene SRSF3 in oral squamous cell carcinoma. *Biochim. Biophys. Acta Mol. Cell Res.* **1865**, 1161–
1093 1172 (2018).
1094 94. She, W., Shao, J. & Jia, R. Targeting splicing factor SRSF6 for cancer therapy. *Front. Cell Dev. Biol.*
1095 **9**, 780023 (2021).
1096 95. Yoh, S. M., Cho, H., Pickle, L., Evans, R. M. & Jones, K. A. The Spt6 SH2 domain binds Ser2-P
1097 RNAPII to direct Iws1-dependent mRNA splicing and export. *Genes Dev.* **21**, 160–174 (2007).
1098 96. Martín, E., Vivori, C., Rogalska, M., Herrero-Vicente, J. & Valcárcel, J. Alternative splicing
1099 regulation of cell-cycle genes by SPF45/SR140/CHERP complex controls cell proliferation. *RNA* **27**, 1557–
1100 1576 (2021).
1101 97. Deng, L. *et al.* MYC-driven U2SURP regulates alternative splicing of SAT1 to promote triple-
1102 negative breast cancer progression. *Cancer Lett.* **560**, 216124 (2023).
1103 98. Fernandopulle, M. S. *et al.* Transcription Factor-Mediated Differentiation of Human iPSCs into
1104 Neurons. *Curr. Protoc. Cell Biol.* **79**, e51 (6 2018).
1105 99. Ratti, A. *et al.* Chronic stress induces formation of stress granules and pathological TDP-43
1106 aggregates in human ALS fibroblasts and iPSC-motoneurons. *Neurobiol. Dis.* 105051 (8 2020)
1107 doi:10.1016/j.nbd.2020.105051.
1108 100. Gasset-Rosa, F. *et al.* Cytoplasmic TDP-43 De-mixing Independent of Stress Granules Drives
1109 Inhibition of Nuclear Import, Loss of Nuclear TDP-43, and Cell Death. *Neuron* vol. 102 339–357.e7
1110 Preprint at (4 2019).
1111 101. Smeltzer, S. *et al.* Hypusination of Eif5a regulates cytoplasmic TDP-43 aggregation and
1112 accumulation in a stress-induced cellular model. *Biochim. Biophys. Acta Mol. Basis Dis.* **1867**, 165939
1113 (2021).
1114 102. Higashi, S. *et al.* TDP-43 associates with stalled ribosomes and contributes to cell survival during
1115 cellular stress. *J. Neurochem.* **126**, 288–300 (2013).
1116 103. McGurk, L. *et al.* Poly(ADP-Ribose) Prevents Pathological Phase Separation of TDP-43 by
1117 Promoting Liquid Demixing and Stress Granule Localization. *Mol. Cell* **71**, 703–717.e9 (9 2018).
1118 104. Colombrita, C. *et al.* TDP-43 is recruited to stress granules in conditions of oxidative insult. *J.*
1119 *Neurochem.* **111**, 1051–1061 (2009).

1120 105. Hans, F., Glasebach, H. & Kahle, P. J. Multiple distinct pathways lead to hyperubiquitylated
1121 insoluble TDP-43 protein independent of its translocation into stress granules. *J. Biol. Chem.* **295**, 673–
1122 689 (2020).
1123 106. Meyerowitz, J. *et al.* C-Jun N-terminal kinase controls TDP-43 accumulation in stress granules
1124 induced by oxidative stress. *Mol. Neurodegener.* **6**, 57 (2011).
1125 107. Cohen, T. J., Lee, V. M. Y. & Trojanowski, J. Q. TDP-43 functions and pathogenic mechanisms
1126 implicated in TDP-43 proteinopathies. *Trends in Molecular Medicine* vol. 17 659–667 Preprint at
1127 https://doi.org/10.1016/j.molmed.2011.06.004 (11 2011).
1128 108. Dasgupta, T. & Ladd, A. N. The importance of CELF control: molecular and biological roles of the
1129 CUG-BP, Elav-like family of RNA-binding proteins. *Wiley Interdiscip. Rev. RNA* **3**, 104–121 (1 2012).
1130 109. Förch, P. *et al.* The Apoptosis-Promoting Factor TIA-1 Is a Regulator of Alternative Pre-mRNA
1131 Splicing. *Molecular Cell* vol. 6 1089–1098 Preprint at https://doi.org/10.1016/S1097-2765(00)00107-6
1132 (11 2000).
1133 110. Gatto-Konczak, F. D. *et al.* The RNA-Binding Protein TIA-1 Is a Novel Mammalian Splicing
1134 Regulator Acting through Intron Sequences Adjacent to a 5' Splice Site. *https://doi. org/10. 1128/MCB.*
1135 *20. 17. 6287-6299. 2000* vol. 20 6287–6299 Preprint at https://doi.org/10.1128/MCB.20.17.6287-
1136 6299.2000 (9 2023).
1137 111. Komor, A. C., Kim, Y. B., Packer, M. S., Zuris, J. A. & Liu, D. R. Programmable editing of a target
1138 base in genomic DNA without double-stranded DNA cleavage. *Nature* **533**, 420–424 (4 2016).
1139 112. Mallory, M. J. *et al.* Signal- and development-dependent alternative splicing of LEF1 in T cells is
1140 controlled by CELF2. *Mol. Cell. Biol.* **31**, 2184–2195 (2011).
1141 113. Mallory, M. J. *et al.* Induced transcription and stability of CELF2 mRNA drives widespread
1142 alternative splicing during T-cell signaling. *Proc. Natl. Acad. Sci. U. S. A.* **112**, E2139–48 (2015).
1143 114. Yanaizu, M., Washizu, C., Nukina, N., Satoh, J.-I. & Kino, Y. CELF2 regulates the species-specific
1144 alternative splicing of TREM2. *Sci. Rep.* **10**, 17995 (2020).
1145 115. Lai, S. *et al.* N6-methyladenosine-mediated CELF2 regulates CD44 alternative splicing affecting
1146 tumorigenesis via ERAD pathway in pancreatic cancer. *Cell Biosci.* **12**, 125 (2022).
1147 116. Ladd, A. N., Charlet, N. & Cooper, T. A. The CELF family of RNA binding proteins is implicated in
1148 cell-specific and developmentally regulated alternative splicing. *Mol. Cell. Biol.* **21**, 1285–1296 (2001).
1149 117. Zhang, W.-J. & Wu, J. Y. Sip1, a novel RS domain-containing protein essential for pre-mRNA
1150 splicing. *Mol. Cell. Biol.* **18**, 676–684 (1998).

1151 118. Zhao, W. *et al.* HuR and TIA1/TIAL1 are involved in regulation of alternative splicing of SIRT1 pre-
1152 mRNA. *Int. J. Mol. Sci.* **15**, 2946–2958 (2014).
1153 119. Izquierdo, J. M. & Valcárcel, J. Two isoforms of the T-cell intracellular antigen 1 (TIA-1) splicing
1154 factor display distinct splicing regulation activities. Control of TIA-1 isoform ratio by TIA-1-related
1155 protein: Control of Tia-1 isoform ratio by Tia-1-related protein. *J. Biol. Chem.* **282**, 19410–19417 (2007).
1156 120. Aznarez, I. *et al.* A systematic analysis of intronic sequences downstream of 5' splice sites reveals
1157 a widespread role for U-rich motifs and TIA1/TIAL1 proteins in alternative splicing regulation. *Genome*
1158 *Res.* **18**, 1247–1258 (2008).
1159 121. Mackenzie, I. R. *et al.* TIA1 Mutations in Amyotrophic Lateral Sclerosis and Frontotemporal
1160 Dementia Promote Phase Separation and Alter Stress Granule Dynamics. *Neuron* **95**, 808–816.e9 (8
1161 2017).
1162 122. Hirsch-Reinshagen, V. *et al.* Clinical and neuropathological features of ALS/FTD with TIA1
1163 mutations. *Acta neuropathologica communications* vol. 5 96 Preprint at
1164 https://doi.org/10.1186/S40478-017-0493-X/FIGURES/5 (12 2017).
1165 123. Osma-Garcia, I. C. *et al.* The splicing regulators TIA1 and TIAL1 are required for the expression of
1166 the DNA damage repair machinery during B cell lymphopoiesis. *Cell reports* vol. 41 Preprint at
1167 https://doi.org/10.1016/J.CELREP.2022.111869 (12 2022).
1168 124. Wang, Y., Liu, J. & Zhou, F. The role of TIA1 and TIAL1 in germinal center B cell function and
1169 survival. *Cell. Mol. Immunol.* **20**, 1090–1092 (2023).
1170 125. Seddighi, S. *et al.* Mis-spliced transcripts generate de novo proteins in TDP-43-related ALS/FTD.
1171 *Sci. Transl. Med.* (1 2024) doi:10.1126/SCITRANSLMED.ADG7162.
1172 126. Sainouchi, M. *et al.* A novel splicing variant of ANXA11 in a patient with amyotrophic lateral
1173 sclerosis: histologic and biochemical features. *Acta Neuropathol Commun* **9**, 106 (2021).
1174 127. Riku, Y. *et al.* TDP-43 Proteinopathy and Tauopathy: Do They Have Pathomechanistic Links? *Int.*
1175 *J. Mol. Sci.* **23**, (12 2022).
1176 128. Vogt, M. A. *et al.* TDP-43 induces p53-mediated cell death of cortical progenitors and immature
1177 neurons. *Sci. Rep.* **8**, 8097 (2018).
1178 129. Walker, A. K. *et al.* Functional recovery in new mouse models of ALS/FTLD after clearance of
1179 pathological cytoplasmic TDP-43. *Acta Neuropathol.* **130**, 643–660 (11 2015).
1180 130. Josephs, K. A. *et al.* TDP-43 is a key player in the clinical features associated with Alzheimer's
1181 disease. *Acta Neuropathol.* **127**, 811–824 (2014).

1182 131. Katsumata, Y., Fardo, D. W., Kukull, W. A. & Nelson, P. T. Dichotomous scoring of TDP-43
1183 proteinopathy from specific brain regions in 27 academic research centers: associations with Alzheimer's
1184 disease and cerebrovascular disease pathologies. *Acta Neuropathol. Commun.* **6**, 142 (2018).
1185 132. Shih, Y.-H. *et al.* TDP-43 interacts with amyloid-β, inhibits fibrillization, and worsens pathology in
1186 a model of Alzheimer's disease. *Nat. Commun.* **11**, 5950 (2020).
1187 133. Donev, R., Newall, A., Thome, J. & Sheer, D. A role for SC35 and hnRNPA1 in the determination
1188 of amyloid precursor protein isoforms. *Mol. Psychiatry* **12**, 681–690 (2007).
1189 134. Bayram, E., Shan, G. & Cummings, J. L. Associations between comorbid TDP-43, Lewy body
1190 pathology, and neuropsychiatric symptoms in Alzheimer's disease. *J. Alzheimers. Dis.* **69**, 953–961
1191 (2019).
1192 135. Wennberg, A. M. *et al.* Association of apolipoprotein E ε4 with transactive response DNA-
1193 binding protein 43. *JAMA Neurol.* **75**, 1347–1354 (2018).
1194 136. Finkel, R. S. *et al.* Nusinersen versus sham control in infantile-onset spinal muscular atrophy. *N.*
1195 *Engl. J. Med.* **377**, 1723–1732 (2017).
1196 137. Mercuri, E. *et al.* Nusinersen versus sham control in later-onset spinal muscular atrophy. *N. Engl.*
1197 *J. Med.* **378**, 625–635 (2018).
1198 138. Bennett, C. F., Krainer, A. R. & Cleveland, D. W. Antisense oligonucleotide therapies for
1199 neurodegenerative diseases. *Annu. Rev. Neurosci.* **42**, 385–406 (2019).
1200 139. Baughn, M. W. *et al.* Mechanism of STMN2 cryptic splice-polyadenylation and its correction for
1201 TDP-43 proteinopathies. *Science* **379**, 1140–1149 (3 2023).
1202 140. Keuss, M. J. *et al.* Loss of TDP-43 induces synaptic dysfunction that is rescued by UNC13A splice-
1203 switching ASOs. *bioRxiv* 2024.06.20.599684 (6 2024) doi:10.1101/2024.06.20.599684.
1204 141. Zhao, W. *et al.* POSTAR3: an updated platform for exploring post-transcriptional regulation
1205 coordinated by RNA-binding proteins. *Nucleic Acids Res.* **50**, D287–D294 (1 2022).
1206 142. Josephs, K. A. *et al.* Updated TDP-43 in Alzheimer's disease staging scheme. *Acta Neuropathol.*
1207 **131**, 571–585 (2016).
1208 143. Tomé, S. O. *et al.* Distinct molecular patterns of TDP-43 pathology in Alzheimer's disease:
1209 relationship with clinical phenotypes. *Acta Neuropathol. Commun.* **8**, 61 (2020).
1210 144. Bionetworks, S. Gene Expression (RNA seq - bulk brain).
1211 https://www.synapse.org/Synapse:syn3388564/version/.

1212 145. Agrawal, S. *et al.* Limbic-predominant age-related TDP-43 encephalopathy neuropathologic
1213 change and microvascular pathologies in community-dwelling older persons. *Brain Pathol.* **31**, e12939
1214 (2021).
1215 146. Agrawal, S. *et al.* Hippocampal neuronal loss and cognitive decline in LATE-NC and ADNC among
1216 community-dwelling older persons. *Alzheimers. Dement.* **21**, e14500 (2025).
1217 147. Vialle, R. A. *et al.* Structural variants linked to Alzheimer's disease and other common age-
1218 related clinical and neuropathologic traits. *Genome Med.* **17**, 20 (2025).
1219 148. Pantazis, C. B. *et al.* A reference human induced pluripotent stem cell line for large-scale
1220 collaborative studies. *Cell Stem Cell* **29**, 1685–1702.e22 (12 2022).
1221 149. Coelho, M. A. *et al.* Base editing screens map mutations affecting interferon-γ signaling in
1222 cancer. *Cancer Cell* **41**, 288–303.e6 (2023).
1223 150. Martin, M. Cutadapt removes adapter sequences from high-throughput sequencing reads.
1224 *EMBnet j.* **17**, 10 (2011).
1225 151. Dobin, A. *et al.* STAR: ultrafast universal RNA-seq aligner. *Bioinformatics* **29**, 15–21 (2013).
1226 152. Köster, J. & Rahmann, S. Snakemake--a scalable bioinformatics workflow engine. *Bioinformatics*
1227 **28**, 2520–2522 (2012).
1228 153. Elinger, D., Gabashvili, A. & Levin, Y. Suspension trapping (S-Trap) is compatible with typical
1229 protein extraction buffers and detergents for bottom-up proteomics. *J. Proteome Res.* **18**, 1441–1445
1230 (2019).
1231 154. Cox, J. & Mann, M. MaxQuant enables high peptide identification rates, individualized p.p.b.-
1232 range mass accuracies and proteome-wide protein quantification. *Nat. Biotechnol.* **26**, 1367–1372
1233 (2008).
1234 155. Carpenter, A. E. *et al.* CellProfiler: image analysis software for identifying and quantifying cell
1235 phenotypes. *Genome Biol.* **7**, (10 2006).
1236 156. Stirling, D. R. *et al.* CellProfiler 4: improvements in speed, utility and usability. *BMC*
1237 *Bioinformatics* **22**, (12 2021).
1238 157. Perez-Riverol, Y. *et al.* The PRIDE database at 20 years: 2025 update. *Nucleic Acids Res.* **53**,
1239 D543–D553 (2025).

1240 160. [126].
1241
1242

1243

1244